

1 The Impact of an ICME on the Jovian X-ray Aurora

William R. Dunn,^{1,2} Graziella Branduardi-Raymont,¹ Ronald F. Elsner,³

Marissa F. Vogt,⁴ Laurent Lamy,⁵ Peter G. Ford,⁶ Andrew J. Coates,^{1,2} G.

Randall Gladstone,⁷ Caitriona M. Jackman,⁸ Jonathan D. Nichols,⁹ I.

Jonathan Rae,¹ Ali Varsani,¹ Tomoki Kimura,^{10,11} Kenneth C. Hansen,¹²

Jamie M. Jasinski^{1,2,12}

¹Mullard Space Science Laboratory,

This is the author manuscript accepted for publication and has undergone full peer review but has not been through the copyediting, typesetting, pagination and proofreading process, which may lead to differences between this version and the Version of Record. Please cite this article as doi:

10.1029/2015JA021888

January 30, 2016, 6:52am

D R A F T

Key Points.

- The arrival of an ICME changes Jupiter's X-ray auroral spectra, spatial and temporal characteristics
- Jupiter's X-ray aurora map to sources in the outer magnetosphere and also to open field lines
- Jupiter's X-ray aurora is produced by at least 2 distinct ion populations during the ICME

Abstract. — We report the first Jupiter X-ray observations planned to coincide with an Interplanetary Coronal Mass Ejection (ICME). At the predicted ICME arrival time, we observed a factor of ~ 8 enhancement in Jupiter's X-ray aurora. Within 1.5 hours of this enhancement, intense bursts of non-10 Io decametric radio emission occurred. Spatial, spectral and temporal characteristics also varied between ICME arrival and another X-ray observation two days later. Gladstone et al. [2002] discovered the polar X-ray hot spot and found it pulsed with 45minute quasi-periodicity. During the ICME arrival, the hot spot expanded and exhibited two periods: 26minute periodicity from sulfur ions and 12minute periodicity from a mixture of carbon/sulfur and oxygen ions. After the ICME, the dominant period became 42minutes. By comparing Vogt et al. [2011] Jovian mapping models with spectral analysis, we found that during ICME arrival at least two distinct ion populations, from Jupiter's dayside, produced the X-ray aurora. Auroras mapping to magnetospheric field lines between 50-70 R_J were dominated by emission from precipitating sulfur ions ($S^{7+, \dots, 14+}$). Emissions mapping to closed field lines

Department of Space & Climate Physics,

18 between 70-120 R_J and to open field lines were generated by a mixture of pre-
19 cipitating oxygen ($O^{7+,8+}$) and sulfur/carbon ions, possibly implying some
20 solar wind precipitation. We suggest the best explanation for the X-ray hot
21 spot is pulsed dayside reconnection perturbing magnetospheric downward
22 currents, as proposed by Bunce et al. [2004]. The auroral enhancement has
23 different spectral, spatial and temporal characteristics to the hot spot. By
24 analysing these characteristics and coincident radio emissions, we propose
25 that the enhancement is driven directly by the ICME through Jovian mag-
26 netosphere compression and/or a large-scale dayside reconnection event.

University College London, Holmbury St.

1. Introduction

27 The Einstein observatory first permitted the identification of Jupiter's X-ray emission
28 during the 1980s [Metzger et al., 1983]. Since then, ROSAT, Chandra and XMM-Newton
29 X-ray observatories have provided the opportunity to study the spatial, spectral and tem-
30 poral characteristics of this X-ray emission in more detail [Waite et al., 1994; Gladstone
31 et al., 1998, 2002; Elsner et al., 2005; Branduardi-Raymont et al., 2004, 2007a, b, 2008;
32 Bhardwaj et al., 2005, 2006]. Jupiter's X-ray emission consists of two components: an
33 equatorial/disk component and a high latitude North and South auroral component [Met-
34 zger et al., 1983; Waite et al., 1994]. The disk emission is found to be dominated by elastic
35 and fluorescent scattering of solar X-ray photons in the upper atmosphere, meaning that
36 changes in the Sun's X-ray emission induce changes in Jupiter's disk emission [Maurel-
37 lis et al., 2000; Branduardi-Raymont et al., 2007b; Bhardwaj et al., 2005, 2006; Cravens
38 et al., 2006]. The majority of the auroral X-ray emission above $\sim 60^\circ$ latitude is thought to
39 be due to charge exchange (CX) interactions between precipitating ions and atmospheric
40 neutral hydrogen molecules [Waite et al., 1994; Cravens et al., 1995, 2003; Cravens and
41 Ozak., 2012]. The origin of the ions, however, has been a matter of debate; they could
42 either come from the magnetosphere or from the solar wind. In this work we explore the
43 question of ion origin and, in particular, we analyse changes to the Jovian X-ray emis-
44 sion during heightened solar wind conditions to better understand the factors driving the
45 emission.

Mary, Dorking, Surrey RH5 6NT, UK

46 Jupiter's Northern X-ray aurora is dominated by two distinctive spectral emissions,
47 which are each associated with distinct spatial emissions:

48 1) The hot spot region containing ion-produced CX soft X-ray line emissions (0.2-2 keV)
49 [Gladstone et al., 2002].

50 2) The electron-produced hard X-ray (greater than 2 keV) bremsstrahlung continuum
51 emission, which appears to overlap the UV main oval region [Branduardi-Raymont et al.,
52 2008].

53

1.1. Soft X-rays and The Hot Spot Region

54 Poleward of the main auroral oval, and therefore magnetically mapping to larger radial
55 distances, is the 'hot spot' region discovered by Gladstone et al. [2002]. This region is
56 found to be the dominant X-ray feature in Jupiter's Northern aurora and appears to be
57 roughly fixed in System III (S3) coordinates of 160° - 180° longitude and 60° - 70° latitude
58 [Gladstone et al., 2002]. Using the VIP4 model [Connerney et al., 1998], Gladstone et al.
59 [2002] mapped the hot spot to magnetospheric origins further than $30R_J$ from the planet.
60 Poleward of regions mapping to $30R_J$ the VIP4 model does not permit accurate mapping
61 of the ionosphere to the magnetosphere [Vogt et al., 2011], so the precise magnetospheric
62 origin of the hot spot remained unknown.

63 Pertinent to understanding the Jovian magnetosphere is the 45 minute periodicity that
64 Gladstone et al. [2002] also detected in the X-ray hot spot. Elsner et al. [2005] and

²The Centre for Planetary Science at

65 Branduardi-Raymont et al. [2004, 2007b] were unable to find strict periodicity in Chandra
66 or XMM-Newton observations in 2003 and 2004, but noted that periodic behaviour may
67 be transient and linked to solar activity.

68 Chandra and XMM-Newton observations have shown that the hot spot emission is
69 dominated by soft X-ray CX spectral lines from ions [Elsner et al., 2005; Branduardi-
70 Raymont et al., 2004, 2007b]. Further, these authors showed that dominant constituents of
71 this emission are fully-stripped and almost fully-stripped oxygen ions, whose CX emission
72 (characterised by strong OVII and OVIII line emission) fits well to the observed 500-900
73 eV spectra. The authors also showed that at lower energies, between 200-400 eV, there
74 are likely to be CX lines from carbon or sulfur ions, but spectral resolution has been
75 insufficient to distinguish between these species.

76 Determining whether the low energy lines are due to carbon or sulfur ions is fundamental
77 to determining whether Jupiter's magnetosphere is open or closed to the solar wind.
78 Carbon and oxygen are the most abundant heavy ions in the solar wind [Cravens, 1997],
79 so a carbon confirmation would suggest a solar wind origin for the emission. Conversely,
80 Jupiter's magnetosphere is dominated by sulfur and oxygen ions, which are produced
81 by Io's volcanoes and diffuse to the outer magnetosphere. A sulfur identification would
82 indicate that these precipitating ions are magnetospheric in origin. While the Jovian
83 magnetosphere is dominated by sulfur and oxygen, these are predominantly in charges
84 states of S^+ , S^{2+} and S^{3+} or O^+ and O^{2+} [Geiss et al., 1992]. For X-ray production by
85 CX, charge states of at least S^{7+} and O^{7+} are required, so the ions require acceleration to
86 enable collisions to strip electrons and generate the higher charge states observed.

UCL/Birkbeck, Gower Street, London,

87 Cravens et al. [2003] proposed two mechanisms capable of explaining the CX emission;
88 one for ions originating in the solar wind and the other for ions originating in the magne-
89 tosphere. If the ions are carbon, then they would already have the required charge state
90 in the solar wind. However, Cravens et al. [2003] show that under normal solar wind
91 conditions, without an acceleration process, the low densities of solar wind ions at Jupiter
92 are only capable of explaining 0.5-5% of the observed emission. A field-aligned potential
93 drop of ~ 200 kV between the magnetopause and upper atmosphere is required to accel-
94 erate the particles to sufficient energies to generate the emission from cusp precipitation
95 alone. At these energies, bright UV emission should be observable from precipitating pro-
96 tons but this is only observed during short-lived flare events [Trafton et al., 1998; Waite
97 et al., 2001]. These bright polar cap UV flares were attributed to the cusp by Pallier and
98 Prangé [2001]. Outside of flares, Cravens et al. [2003] found that cusp precipitation could
99 only be partially responsible for the emission. Instead, they favoured a mechanism where
100 field-aligned electric potentials (of at least 8 MV) in the outer magnetosphere accelerate
101 local sulfur and oxygen ions to the required energies. The location of downward currents
102 in this region is also supported by work by Nichols [2011].

103 Bunce et al. [2004] proposed an alternative scenario. They suggested that pulsed dayside
104 reconnection at the magnetopause could generate the observed X-ray emission. They
105 showed that this would lead to the precipitation of solar wind ions, but that it actually
106 drives more intense X-ray emission from closed outer magnetosphere field lines that are
107 perturbed by reconnection flows. This would mean that the greater emission intensity
108 would be from sulfur in the outer magnetosphere. The authors also indicated that pulsed

WC1E 6BT, UK

D R A F T

January 30, 2016, 6:52am

D R A F T

109 reconnection could explain the period observed by Gladstone et al. [2002], suggesting that
110 a 30-50 minute period would be expected from this process. Bonfond et al. [2011] suggest
111 that the quasi-periodic UV flaring with timescales of 2-3 minutes found poleward of the
112 main oval, in a region close to the X-ray hot spot, may also be caused by pulsed dayside
113 reconnection.

114 When investigating the Jovian X-ray aurora spectra, Branduardi-Raymont et al.
115 [2004, 2007b] and Elsner et al. [2005] showed a slight preference for sulfur and there-
116 fore a magnetospheric origin, but Elsner et al. [2005] concluded that they were unable to
117 rule-out carbon. Further modelling [Hui et al., 2009, 2010; Kharchenko et al., 2006, 2008;
118 Ozak et al., 2010, 2013] has demonstrated that a good fit to the spectra can be found
119 with a combination of 1-2MeV/amu oxygen and sulfur ion lines. Hui et al. [2010] also
120 found that the majority of spectra could be well fitted without carbon lines, although one
121 set of spectra had a better fit with a carbon-oxygen model. They also noted significant
122 variation between observation dates and between Northern and Southern auroras. This
123 North-South pole variation may be expected because Jupiter's 9.6° dipole tilt ensures that
124 the viewing geometry of one pole is always significantly impaired relative to the other.
125 This means that additional spatial features (and the spectral lines associated with them)
126 can be viewed more clearly for one pole than the other. Additionally, the magnetic field
127 footprints in the North Pole feature a significant kink structure between 90° - 150° S3 lon-
128 gitude [Pallier and Prangé, 2001], which is well fitted by a magnetic anomaly [Grodent

³ZP12, NASA Marshall Space Flight

129 et al., 2008]; this is absent from the South pole, which may relate to its more diffuse X-ray
130 emission [Elsner et al., 2005].

1.2. Hard X-rays and The Main Oval

131 Equatorward of the hot spot is the UV main oval. By comparing Chandra auroral X-
132 ray events, Branduardi-Raymont et al. [2008] showed that hard X-rays (energies greater
133 than 2 keV) map well to the main UV oval. This emission is found to be well fitted by
134 bremsstrahlung radiation from precipitating electrons [Branduardi-Raymont et al., 2007b],
135 implying a spatial coincidence of the X-ray and UV emitting electron populations.

136 The main oval is well evidenced as mapping to 20-30 R_J [Vogt et al., 2011], where upward
137 field-aligned currents in the corotation breakdown region could generate downward precip-
138 itation of 20-100keV electrons [Hill, 2001; Cowley and Bunce, 2001; Nichols and Cowley,
139 2004]. This region is significantly separated from the 63-92 R_J standoff distance calculated
140 by Joy et al. [2002] and thus emission might not be expected to be directly influenced by
141 the solar wind. However, in contrast with this apparent isolation, Branduardi-Raymont
142 et al. [2007b] note that in 2003 XMM-Newton observations showed that both hard and
143 soft X-ray emissions varied at a time of increased solar activity [Branduardi-Raymont
144 et al., 2004, 2007b]. UV main emissions connected with the hard X-ray emission are also
145 known to be modulated by the solar wind [Pryor et al., 2005; Nichols et al., 2007; Clarke
146 et al., 2009; Nichols et al., 2009].

Center, USA

1.3. Connecting Solar Wind and Auroral Variations

147 While the impact of a southward-turning Interplanetary Magnetic Field and the pressure
148 pulse induced by an Interplanetary Coronal Mass Ejection (ICME) on the Earth's aurora
149 are known to produce auroral brightening [Elphinstone et al., 1996; Chua et al., 2001],
150 the impact on Jupiter's larger magnetosphere is not well understood. There are two key
151 challenges associated with examining relationships between solar wind conditions and the
152 Jovian aurora. Firstly, the timescales for the propagation of a solar wind induced shock
153 through the Jovian magnetosphere are not well-understood. Secondly, without in-situ
154 measurements of the solar wind conditions close to Jupiter, we rely on propagation models
155 to estimate the solar wind conditions upstream of Jupiter. The propagation of the solar
156 wind beyond the inner heliosphere becomes increasingly complex, meaning that outside
157 of certain limiting conditions (e.g: Jupiter in opposition) the uncertainty associated with
158 propagation models can be of the order of days, making it difficult to precisely correlate
159 solar activity with auroral intensification. However, Gurnett et al. [2002] found that
160 Jovian hectometric radio emission bursts (0.3-3MHz) coincided with maxima in solar
161 wind density. Prangé et al. [2004] and Lamy et al. [2012] have used these enhancements
162 in radio emission to trace the progress of ICME induced shocks through the solar system.
163 Further, Echer et al. [2010]; Hess et al. [2012, 2014] found that non-Io decametric radio
164 emission bursts are correlated with periods of increased solar wind dynamic pressure.

165 Jupiter's auroral variations in response to changes in solar wind pressure are well cat-
166 alogued at other wavelengths [Barrow et al., 1986; Ladreiter and Leblanc, 1989; Kaiser,

⁴Center for Space Physics, Boston

167 1993; Prangé et al., 1993; Baron et al., 1996; Zarka, 1998; Pryor et al., 2005; Nichols et al.,
168 2007; Clarke et al., 2009; Nichols et al., 2009; Hess et al., 2012, 2014] but X-ray emission is
169 yet to be investigated in this manner. In particular, there have been few previous oppor-
170 tunities to connect X-ray observations of high-latitude precipitating ions with solar wind
171 conditions. There has also been limited analysis of how the spatial morphology of X-ray
172 features vary over time. In the current work, we analyse auroral spatial features, con-
173 nect them with spectral features and compare their morphology and evolution over time
174 to better understand how solar wind conditions and local time magnetosphere variation
175 might drive them.

176 In section 2, we consider the propagation of an ICME to Jupiter and describe how
177 two Chandra X-ray observations and radio measurements were timed to coincide with
178 the expected arrival time of the ICME at the planet. In section 3, we present polar
179 projections of the X-ray events, identifying changes in their spatial distribution between
180 the observations. In section 4, we compare the auroral lightcurves for each observation
181 and find connections between a bright X-ray auroral enhancement and decametric radio
182 emission thought to be induced by the ICME. In section 5, we compare the spectra for
183 the hot spot and the auroral enhancement, identifying changes between the observations,
184 which are possibly induced by the ICME. We then compare the X-ray polar projections
185 for specific energy ranges (section 6), based on the different precipitating particles species
186 generating the emission. For instance, we provide polar projections for X-ray emission
187 only from oxygen ions, in order to compare this with other ion species and electrons.
188 By doing this, we find that there is an X-ray auroral region closer to the UV main oval

University, USA

D R A F T

January 30, 2016, 6:52am

D R A F T

189 that is dominated by emission from high charge-state ions of sulphur or carbon. While
190 poleward of this, the population is more of a mixture of high charge-state oxygen and
191 high charge-state carbon/sulphur ions. In section 7, we bin the X-ray events based on
192 the timing of specific sub-solar longitudes (noon times) and use these to identify how
193 auroral developments relate to the evolution of the magnetosphere. Using the Vogt et al.
194 [2011] model, we map the magnetospheric source and local time dependencies of the hot
195 spot region and the auroral enhancement region. This indicates to what extent X-ray
196 emission may be driven by the opening/closing of magnetic field lines, the location of
197 the Sun relative to Jupiter's magnetosphere and the magnetosphere's auroral footprints.
198 In section 8, we investigate periodicities in the X-ray emission and their relationships to
199 specific ion species. In sections 9, 10 and 11 we summarise results, provide discussion on
200 these and draw conclusions.

2. October 2011 Jupiter Observations

201 The two Chandra X-ray observations reported here were undertaken to attempt to
202 establish if and to what extent the solar wind drives Jupiter's X-ray aurora. Having
203 previously observed variations in X-ray emission possibly associated with increased solar
204 activity [Branduardi-Raymont et al., 2007b], an extreme solar event such as an ICME was
205 thought to provide the opportunity to better understand this connection. To minimise the
206 uncertainty associated with models that propagate the solar wind conditions to Jupiter
207 and to maximise the X-ray flux and spatial resolution, it is important that Jupiter is

⁵LESIA, Observatoire de Paris, CNRS,

208 observed close to opposition, with the smallest possible Earth-Sun-Jupiter angle. Opposi-
209 tion occurred in October 2011, so a Chandra Target of Opportunity (TOO) proposal was
210 submitted to observe Jupiter at the time when an ICME was predicted to arrive.

211 We used the 1.5-D MHD mSWiM model (<http://mswim.engin.umich.edu/>) [Zieger and
212 Hansen, 2008] to determine the Solar Wind parameters at Jupiter. This allowed us to
213 propagate solar wind measurements from 1 AU to Jupiter. Inspection of the solar wind
214 density, velocity and the Interplanetary Magnetic Field (IMF) timelines (Figure 1) indi-
215 cated the predicted arrival of an ICME at Jupiter over the 2nd and 3rd of October 2011,
216 Day of Year (DoY) 275-276 (figure 1). At this time, the Earth-Sun-Jupiter angle was $\sim 25^\circ$
217 and Jupiter was ~ 4.07 AU from the Earth, meaning that the propagation model offered a
218 relatively low uncertainty of 10-15 hours and that Jupiter was within the angular extent
219 of the ICME [Robbrecht et al., 2009a, b]. To account for this uncertainty we smooth the
220 mSWiM propagations over a 30 hour moving average.

221 The most accurate parameter is solar wind velocity, followed by density and the tan-
222 gential component of the magnetic field (B_T) [Zieger and Hansen, 2008], which points
223 toward the cross product of the solar rotation vector and the direction radially away from
224 the Sun towards Jupiter. Inspecting the mSWiM model propagations of the solar wind
225 reveals an increase in density from 0.03 n cm^{-3} on DoY 274.5 to a peak of 0.21 n cm^{-3}
226 on DoY 276.75 (figure 1a). Density then decreases from this peak back to a minimum
227 of 0.015 n cm^{-3} on DoY 279.0. The median densities measured upstream of Jupiter by
228 Pioneer 11, Voyager 1 and 2 were 0.13, 0.14 and 0.15 n cm^{-3} respectively, indicating that
229 the mSWiM averaged solar wind density is above the median value [Jackman and Arridge

UPMC, Université Paris Diderot, Meudon,

230 , 2011](see supplementary materials for these distributions). There is also a modest in-
231 crease in solar wind velocity during this time from 490 km/s on DoY 274.5 to 500 km/s
232 on DoY 276.0 (figure 1b). This then decreases gradually to 450 km/s by DoY 279.0. These
233 solar wind velocities are similar to the median velocity upstream of Jupiter measured by
234 Pioneer 11 (493 km/s), but represent an increase over the Voyager 1 and 2 median veloci-
235 ties (439 and 441 km/s respectively). The mSWiM predicted density and velocity is much
236 closer to the mean from Pioneer 11, Voyager 1 and 2 upstream measurements (0.26, 0.23
237 and 0.25 n cm^{-3} and 497, 446 and 448 km/s respectively), suggesting that the variation
238 in solar wind conditions represent a more modest ICME.

239 The B_T magnetic field plot appears to show a rotation in the solar wind magnetic field
240 at this time, with the field oriented in the positive B_T direction from DoY 274.5 to DoY
241 277 and a negative B_T direction from DoY 277 to 280, before returning to a positive
242 orientation again (figure 1c). This variation in IMF along with the simultaneous increase
243 in density and velocity, is consistent with an ICME with flux rope-like interior structure
244 [Hanlon et al., 2004].

245 We also note that the mSWiM model shows that a much stronger ICME was incident at
246 Jupiter from DoY 268 to 272 and the solar wind can be seen to be returning to non-ICME
247 conditions from DoY 272.5. The arrival of this preceding ICME is also accompanied by
248 bursts of Jovian radio emission [Lamy et al., 2012]. It is possible that this preceding ICME
249 may also have driven changes in the Jovian magnetosphere, which are still observable in
250 the X-ray observations reported here.

France

2.1. Chandra X-ray Observations

251 Based on the predicted arrival of the ICME at Jupiter, two TOO observations were
252 made by the Chandra X-ray Observatory (CXO) Advanced CCD Imaging Spectrometer
253 (ACIS). Each observation lasted 11 hours, providing coverage of at least one full Jupiter
254 rotation ($\sim 9\text{h}55\text{m}$). Two observations separated by a couple of days were requested in
255 order to optimise our chances to observe Jupiter during the ICME impact and during
256 relaxed conditions. Both observations were made with the back-illuminated (S3) CCD,
257 which has the highest sensitivity to low-energy X-rays. To simplify the analysis, the
258 observatory was oriented so that the moving image of Jupiter remained on the same
259 output node of the CCD throughout each observation. The first observation was timed
260 to coincide with the predicted arrival of the ICME at Jupiter and lasted from $\sim 21:55$ on
261 the 2nd October to 09:30 on the 3rd October 2011 (Day of Year 275.9-276.4). The second
262 observation ran from 14:35 on the 4th October until 02:20 on the 5th October 2011 (Day
263 of Year 277.6-278.1). Figure 1 shows the times of these observations between red (first
264 observation) and blue (second observation) dotted lines plotted onto the mSWiM solar
265 wind propagation diagram. These suggest that the density peak occurred towards the
266 end of the observation. The second observation occurred when solar wind density was
267 returning to conditions outside of an ICME-induced shock. Figure 1c also shows that the
268 tangential component of the solar wind magnetic field was aligned in an opposite direction
269 for the two observations. However, we note that the 10-15 hour uncertainty could lead
270 features to be shifted into or out of the observations.

⁶Kavli Institute for Astrophysics and

271 The ability of ACIS to detect soft X-rays from optically bright, extended targets is
272 hampered by substantial transmission through its optical blocking filters (OBFs) at wave-
273 lengths between 0.8 and 0.9 μm . Jupiter at opposition fills some 6000 pixels of an ACIS

Space Research, MIT, Cambridge MA, USA

⁷Space Science & Engineering Division,
Southwest Research Institute, San Antonio,
Texas, USA

⁸Department of Physics & Astronomy,
University of Southampton, Southampton
SO17 1BJ, UK

⁹Department of Physics & Astronomy,
University of Leicester, Leicester UK

¹⁰Institute of Space and Astronautical
Science, Japan Aerospace Exploration
Agency, Sagamihara, Japan.

¹¹Nishina Center for Accelerator-Based
Science, RIKEN, 2-1, Hirosawa, Wako,
Saitama, Japan

¹²Department of Atmospheric, Oceanic
and Space Sciences, University of Michigan,
Ann Arbor, Michigan, USA

274 CCD. In the 1999-2000 observations, each of these pixels received an average charge equiv-
275 alent to a 140 eV X-ray. The value has gradually decreased since then - due most probably
276 to contamination buildup on the OBFs. By November 2014, it had fallen to ~ 70 eV/pixel,
277 as estimated from observations of Betelgeuse.

278 To distinguish X-rays from charged particles passing through the CCDs, an on-board
279 digital filter scans the charge distribution in each CCD image, seeking local maxima
280 surrounded by charge patterns peculiar to X-rays. The extra optical signal turns all
281 genuine X-ray events into non-events, which are never reported to the ground. The
282 solution, outlined in Elsner et al. [2005], has been to (a) take CCD bias frames with
283 Jupiter out of the field-of-view, and (b) increase the digital filter's threshold levels by 140
284 eV, allowing the software to compensate for the optical signal. During subsequent ground
285 processing, the 5x5 block of pixels reported for each event candidate are used to subtract
286 the background charge, including the optical signal.

287 If the optical contamination were exactly 140 eV/pixel, the energy of an X-ray could
288 be recovered without any additional systematic error. In practice, Jupiter exhibits strong
289 limb darkening in the near infrared, and most Jovian X-ray emission comes from the polar
290 regions which are observed close to the limb. Also, the optical Point Spread Function
291 (PSF) of the Chandra mirrors is strongly diffracted by the inter-mirror gaps, adding to
292 the limb darkening. The result is that some low-energy X-rays, especially those whose
293 charge is split between pixels, are still filtered out. The loss incurred has been estimated
294 by reprocessing a group of 8 ACIS observations (a total of 104 ks) of the supernova
295 remnant E0102-72.3 - an extended source similar in angular size to Jupiter, which exhibits
296 a strong low- energy thermal bremsstrahlung component - adding successive levels of

297 'optical' contamination, and measuring the resulting change in low-energy spectral flux.
298 The correction came to less than 1% for X-rays above 600 eV, $5\pm 1\%$ at 430 eV, and
299 $10\pm 2\%$ at 220 eV, below which energy the sensitivity of the ACIS CCDs drops off rapidly.
300 To account for this we applied a correction to the auroral spectra (section 5).

2.2. Radio Observations

301 Alongside Chandra X-ray observations, a series of multi-instrument, multi-planet obser-
302 vations were conducted and were initially reported in Lamy et al. [2012], including radio
303 observations of Jupiter during the same interval. Using both ground-based observations,
304 from the Nançay decameter array, and space-based observations, from WIND, STEREO
305 A and B, Jupiter was found to display intensifications of auroral decametric to hectomet-
306 ric emission close to 3 successive ICMEs, the second of which is investigated here. These
307 enhancements driven by the solar wind activity were consistent with those evidenced by
308 [Gurnett et al., 2002] for hectometric emission with Galileo and more recently by [Hess
309 et al., 2012, 2014] for decametric to hectometric emission from Galileo, Cassini and Nançay
310 observations.

311 The radio observations obtained at the time of the Chandra observations (Figure 2) were
312 shifted to account for light travel-time from Jupiter to Earth. Since non-Io decametric
313 radio emission has been found to be correlated with solar wind pressure [Hess et al.,
314 2012, 2014], investigating this radio emission helps to constrain the arrival time of the
315 ICME-induced shock.

316 non-Io decametric emission is arc shaped in the time-frequency plane and the shape
317 of this arc is indicative of the side of the magnetosphere from which it originates. The
318 vertex-early or vertex-late curvature of these arcs indicates whether the emission source

319 was located westward (Jovian dawn) or eastward (Jovian dusk) of the observer (in the
320 direction of Earth). Hess et al. [2012, 2014] showed that forward shocks (where the
321 magnetosphere may be compressed by increased solar wind pressure) are often followed
322 by emission from only one side of the magnetosphere. They showed that reverse shocks
323 (where the solar wind pressure decreases and the magnetosphere may expand) are often
324 followed by emission from both sides of the magnetosphere (i.e: both vertex early and
325 vertex late emission would be observed). At DoY \sim 276.3 and 276.7, STEREO A and B
326 data showed two bursts of decametric emission with only vertex early morphology, which
327 suggests the incidence of two solar wind forward shocks at these times. The first of these
328 two bursts coincided with our first X-ray observation, occurring 2.5 hours (0.1DoY) before
329 the end of the observation (see Figure 2). At \sim 276.2 there is also a fainter burst of non-Io
330 decametric emission.

331 Two additional radio bursts also featured in the STEREO data: a burst of Io-D deca-
332 metric emission at 276.0 and a less intense burst which was only observed by STEREO
333 B (where both spacecraft observed the other bursts) and was difficult to distinguish be-
334 tween Io and non-Io decametric emission at DoY 277.7. This second indistinguishable
335 burst occurred one Io orbit after the burst on DoY 276.0, which may suggest Io is the
336 source. If Io is not the source, then it may suggest that a magnetospheric disturbance has
337 been maintained over 1 Jupiter rotation and that Jupiter's magnetosphere is therefore not
338 completely quiet during the second observation. A corresponding auroral X-ray enhance-
339 ment would go undetected for the burst on DoY 276.0 because the auroral footprints had
340 not rotated into view at this time. It would also be very difficult to distinguish the burst

341 on DoY 277.7, since the auroral footprint will have been on the limb of the Jovian disk
342 at this time.

3. North Pole Projections

343 Using the technique applied in Gladstone et al. [2002], Elsner et al. [2005] and
344 Branduardi-Raymont et al. [2008], time-tagged Chandra X-ray events were re-registered
345 into Jupiter's System III (S3) (1965) spherical latitude-longitude coordinates centred on
346 the rotation poles. Hence, a sky-projected disk of $1.01R_J$ was used for both observations
347 (shown in supplementary materials). It should be noted that when re-registering to S3
348 coordinates, events emitted close to the limb of the Chandra-facing disk will have larger
349 spatial uncertainties because of the increased obliquity of the planet's surface relative to
350 the observer.

351 We estimated spatial uncertainties on events based on Chandra's spatial resolution, by
352 perturbing the Jupiter-centred disk by 2 pixels in the x and y direction, then re-registering
353 the events into S3 coordinates.

354 To identify the spatial distribution of auroral X-rays for the two observations, we present
355 projections looking down onto the rotational North Pole of Jupiter. Figure 3 shows these
356 projections for both observations. Figure 4 shows counts vs latitude plots to quantify the
357 latitudinal concentrations of X-rays. During these observations the South Pole emission
358 was obscured by the viewing geometry, so we focus on the North Pole projections only.

359 We observe a range of differences in the spatial distribution of X-rays between the ob-
360 servations (figures 3 & 4). A surprising difference is a broad bright auroral enhancement
361 in the first observation between 180° - 270° longitude and above 60° latitude. The emission
362 in this area is much dimmer in the second observation. This enhancement is signifi-

363 cantly spatially separated from the hot spot (S3 Longitude: 160° - 180° , Latitude 60° - 70°
364 [Gladstone et al., 2002; Elsner et al., 2005; Branduardi-Raymont et al., 2008]), where the
365 brightest X-ray emission was previously observed. The region above 60° latitude and with
366 longitudes 180° - 270° features 201 ± 14 X-ray counts in the first observation compared to
367 76 ± 9 counts in the second.

368 Given the changing solar wind conditions throughout the observations (section 2) and
369 our lack of knowledge concerning the processes governing both the hot spot and the auroral
370 enhancement, we shall analyse the two separately. We refer to the 90° - 180° longitude
371 quadrant as the ‘Hot Spot Quadrant’ (HSQ) and to the quadrant between 180° - 270°
372 longitude as the ‘Auroral Enhancement Quadrant’ (AEQ). However, we note that there
373 is brightening across both quadrants and that this may be connected.

374 We focus first on the HSQ. For both observations, the majority of the auroral emission
375 (above 60° latitude) occurs poleward of the $30R_J$ contour (the inner red oval on figure 3),
376 indicating that the precipitating particles originate further away from Jupiter than this.
377 The whole region of the HSQ inside the $30R_J$ contour contains 113 ± 11 counts in the first
378 observation compared to 78 ± 9 counts in the second. Previously [Gladstone et al., 2002;
379 Elsner et al., 2005], the hot spot was defined as located between 160° - 180° S3 longitude and
380 60° - 70° latitude, where we find 52 ± 7 counts in the first observation and 37 ± 6 counts in the
381 second observation. We find that the Hot Spot appears to spread out spatially in the first
382 observation. The outer edge of the hot spot (at longitudes 150° - 160° and latitudes 55° -
383 60°) is where the greatest change occurs, with 55 ± 7 X-ray counts in the first observation
384 compared to 28 ± 5 counts in the second. This changing emission occurs between the $30R_J$
385 contour and the hot spot, in a region which during a 2007 HST observing campaign was

386 where the poleward edge of the UV main oval was observed [Nichols et al., 2009]. The
387 second observation appears to have its events much more concentrated in the previously
388 defined hot spot. UV observations have shown that when solar wind compression regions
389 onset, the UV auroras brighten in the ‘active region’ close to this X-ray region, near noon
390 and poleward of the main oval [Grodent et al., 2003; Nichols et al., 2007].

391 For the Auroral Enhancement Quadrant, the first observation displays additional bright
392 features with respect to the second. The difference is most evident in Figure 4, which
393 shows the emission is up to a factor of 5 brighter across all latitude regions from 55° - 85°
394 during the first observation relative to the second. Additionally, Figure 4 shows that in the
395 first observation the levels of emission observed in the AEQ are comparable to those in the
396 same latitude range in the HSQ. Comparing the changes in counts for the HSQ and AEQ
397 could suggest that the HSQ is less sensitive to the ICME than the AEQ. Alternatively, it
398 could suggest that the changes the ICME drives in the X-ray aurora develop with time or
399 with varying solar wind parameters - as Jupiter rotates, the HSQ is visible first and the
400 AEQ rotates into view slightly later (Figure 5).

401 One other aspect of note from the HSQ latitude-counts plot (Figure 4) is that there ap-
402 pears to be increased emission from the disk/equatorial region. This suggests the presence
403 of increased solar X-ray flux, which is fluoresced and elastically scattered in the Jovian
404 atmosphere. The occurrence of a solar flare at a time consistent with the increase is con-
405 firmed by inspection of GOES X-ray lightcurves (see supplementary material). Analysis
406 of the polar projections for discrete energy regimes (section 3.3) shows that the flare is not
407 a significant contributing factor for the increased auroral emission, ensuring the validity
408 of the changing auroral activity. We note that this Solar Flare is a distinct event from the

409 ICME and directly introduces additional solar X-ray photons to the Jovian disk, while
410 the ICME introduces X-rays indirectly.

4. Auroral X-ray Lightcurves

411 To generate the auroral X-ray lightcurves we took those events which occurred above
412 S3 latitudes of 60° in the polar projections (section 3) and placed them into 1 minute
413 time bins. We then shifted the lightcurves to account for Jupiter-Earth light travel time.
414 During the first observation, the X-ray emission was brighter and more variable with
415 multiple enhancements that contain twice as many counts as similar enhancements in the
416 second observation. To distinguish between variation in emission from the HSQ and the
417 AEQ, we produced separate lightcurves for each quadrant (figure 5). To help identify any
418 local time dependencies, we also indicate the sub-solar longitude (SSL) corresponding to
419 the timing of the observations.

420 Figure 5 shows that the first half of each observation was dominated by the hot spot.
421 In the first observation, the hot spot became visible shortly before DoY 276.04 and 80°
422 SSL and the counts increased by up to a factor of 6, from ~ 4 counts/ks to peaks of 19-27
423 counts/ks. For the second observation the hot spot appeared on the face before DoY
424 277.7 and the counts increased by up to a factor of 4.5, from 4 to 18 counts/ks.

425 The AEQ shows the most striking difference between the lightcurves. The second
426 observation was generally quiet, with ~ 3 -5 counts/ks, with the exception of a single peak
427 containing 9 counts/ks at 277.93. In contrast, the first observation contained a prominent
428 single peak of 33 counts/ks at DoY 276.24, which lasted 15-25 minutes and was higher
429 than the peak emission from the hot spot. Prior to the peak, there was a gradual increase
430 from DoY 276.2 to 276.22. After the peak there was an abrupt drop to 17 counts/ks and

431 then a gradual decrease for 0.1 DoY afterwards, as the region rotated out of view. From
432 the moment the region began to be observable it was emitting 6 counts/ks, while in the
433 second observation it emitted only 1-2 counts/ks, suggesting that the whole region was
434 brighter throughout the first observation.

435 The peak of the enhancement occurred 1-1.5 hours before the non-*Io* decametric radio
436 burst at DoY ~ 276.3 (indicated on figure 5 by the dashed line). We also note that the
437 fainter burst of non-*Io* decametric emission at DoY 276.2 coincides well with the preceding
438 peak on the AEQ auroral lightcurve, suggesting a further possible connection between
439 X-ray emission and non-*Io* decametric emission. The previously recognised connections
440 between this non-*Io* decametric emission and forward shocks induced by ICMEs [Hess
441 et al., 2012, 2014] suggest that the heightened X-ray emission is also likely to be directly
442 connected with the ICME.

443 We also detect periodicity in these lightcurves on the order of 10s of minutes for both
444 observations and this is discussed and analysed in section 8.

5. Auroral Spectra

5.1. Spectral Extraction and Modelling

445 For analysis of the Chandra spectra we divided Jupiter's observed disk emission into
446 three sections: a Northern auroral zone, an equatorial region and a Southern auroral zone
447 (see supplementary materials for regions selected). Given the limited visibility of the
448 Southern aurora, only the Northern aurora is presented.

449 Using the CIAO software package (provided by the Chandra X-ray Center), we followed
450 the standard procedures to extract spectra, which were then analysed using the XSPEC
451 package [Arnaud, 1996]. We applied a correction to the effective area to account for the

452 increased energy thresholds applied within ACIS to circumvent optical light leaks through
453 the OBFs (as discussed in section 2.1). To do this we weighted energies below 0.7 keV
454 based on fitting for the signal degradation to E0102-72.3, which provided a best fit curve
455 of $1 - Y * (x - 0.7) * *2$ with $Y = 0.50$ and $x =$ the energy of channel.

456 We again treated the HSQ and AEQ separately. To do this, we separated each observa-
457 tion into two halves based on the time at which the emission from the hot spot dimmed
458 (figure 5). The spectrum for the first (second) observation HSQ was produced at Jupiter
459 from DoY 275.95 - 276.15 (277.6 - 277.8) UT, while the AEQ events occurred from DoY
460 276.15 - 276.35 (277.8 - 278) UT. The time intervals were selected to maximise exposure
461 times of the given quadrant, while minimising contamination from the other. Figure 6
462 (left) compares the HSQ spectra, and figure 6 (right) those from the AEQ, for the two
463 observations.

464 We fitted the spectra between 240-2000 eV, with a combination of lines with half widths
465 fixed at 20 eV. This produced two challenges. Firstly, the low count rates and large error
466 bars produced unrealistically low reduced χ^2 values of 0.4-0.6 (for 105-111 degrees of
467 freedom). Secondly, Chandra's spectral resolution and energy cutoff at ~ 210 eV lead
468 us to ignore the region from 210-250 eV, since the sharp drop in counts in this region
469 inhibited good fitting. Table 1 and Figure 6 show the best fits.

5.2. Spectral Analysis

470 Inspecting the HSQ spectra (Figure 6a and 6b) first. Both observations featured a large
471 peak between 250-350eV, which could be from sulfur and/or carbon ions.

472 Between 500-900 eV there were a range of oxygen lines. Both observations contained
473 lines near 600 eV and between 700-730 eV, which are likely to be from OVII and possibly

474 also OVIII transitions. The first observation showed an additional spectral line at ~ 860
475 eV, which could have either been from O VIII transitions or evidence for solar X-ray
476 scattering from the disk. While the best fit model contained only one line at 730 eV, we
477 were also able to obtain similar reduced χ^2 values by fitting two lines at ~ 700 eV (OVII)
478 and ~ 780 eV (OVIII), which may suggest the additional line at 860 eV was also an OVIII
479 transition.

480 As mentioned in section 3, a solar X-ray flare reached Jupiter during the time covered by
481 this spectrum (see supplementary materials for further details) and may have imprinted
482 solar lines onto the spectrum. The additional emission above 700 eV could have been
483 from Fe XVII, Fe XXI or Ne X solar photons or a combination of oxygen and solar
484 photons. We also observed a Magnesium (Mg XI) line in the spectra near 1350 eV,
485 which would be expected from a solar flare [Branduardi-Raymont et al., 2007a; Bhardwaj
486 et al., 2005, 2006]. These solar features are absent or much less relevant in the AEQ and
487 throughout the second observation.

488 For the AEQ, the difference between the spectra of the two observations is clear (Figure
489 6c and 6d). The first shows a prominent peak between 200-300eV that appears to be
490 3-4 times higher for the first observation than the second. We were unable to model this
491 accurately because of the low energy cut-off and low spectral resolution, meaning that
492 comparing fluxes and differentiating between sulfur and carbon was not possible. Between
493 300-500 eV there are additional transitions of carbon or sulfur which don't appear in the
494 HSQ spectra or the AEQ spectrum for the second observation.

495 The morphology of the AEQ spectrum between 380-700 eV is particularly interesting.
496 The emission between 550-600 eV is mostly OVII and the line appeared to be asymmetric,

497 with a sharp decline after 600 eV, which led the fit to underestimate the flux for this line in
498 table 1. This region of the spectrum is similar to that of comets Linear S4 and McNaught-
499 Hartley displayed by Elsner et al. [2005]. This similarity to cometary solar wind charge
500 exchange spectra could suggest a solar wind origin for some of the precipitating ions.

501 The 775 eV line appeared to be a good match for the OVIII transition. GOES data
502 (supplementary material) shows that the heightened solar X-ray flux from the first half of
503 the observation was returning to normal at these times, so it is unlikely that solar photons
504 caused the 700-900 eV morphology in this spectrum.

505 For the AEQ in the second observation, the spectrum is best fitted by a set of low flux
506 sulfur/carbon and oxygen lines. Some of this emission may be contamination from the
507 HSQ, which was still partially visible during these times.

6. Connecting Spatial and Spectral Features

508 Given that Chandra's spectral resolution is insufficient to definitively separate between
509 the spectral lines of carbon and sulfur ions, we now examine the auroral morphology
510 in different energy bands. By combining this with magnetic field mapping, we tried to
511 establish the magnetospheric or solar wind origins for specific ion species. To do this, we
512 binned X-rays into four broad energy bins for: carbon/sulfur; oxygen; solar X-ray lines
513 and Hard X-rays. We then plotted the polar projections for each energy range separately.
514 The specific energy ranges were chosen based on a) the ease with which regions could be
515 differentiated in the spectrum; b) the relevant spectral lines for different species [Elsner
516 et al., 2005]; c) Chandra's energy resolution limitations, d) by considering the solar X-ray
517 lines from the equatorial region spectrum.

518 We estimated the carbon or sulfur emission from the spectra between $\sim 200\text{-}500\text{eV}$. We
519 found that photons below 300eV mapped almost exclusively to the auroral zone, with
520 very little disk component (figure 7), so we included these photons in our analysis. The
521 oxygen emission was defined by the band $\sim 500\text{-}800\text{eV}$ from spectral fitting of strong
522 OVII and OVIII lines [Branduardi-Raymont et al., 2004, 2007b; Elsner et al., 2005]. We
523 considered the $\sim 800\text{-}1500\text{eV}$ emission to come from fluoresced or scattered solar pho-
524 tons because this energy range contains the peak of the disk spectrum [Bhardwaj et al.,
525 2005, 2006; Branduardi-Raymont et al., 2007a]. It should be noted that some OVIII lines
526 from completely stripped oxygen [Elsner et al., 2005] also fall in this energy range and may
527 contribute some of the observed auroral emission. Finally, we consider $1500\text{-}5000\text{eV}$ emis-
528 sion to be hard X-rays from precipitating electrons generating bremsstrahlung radiation
529 [Branduardi-Raymont et al., 2007b, 2008].

530 We look first at the polar projections of $200\text{-}500\text{eV}$ carbon/sulfur X-ray events (figure7a)
531 and find that for both observations almost all emission originated in the aurora, with very
532 little equatorial emission. This confirms that the changing emission in this part of the
533 spectra was unrelated to solar flares. We find that carbon/sulfur is the source of the
534 brightening on the edge of the hot spot, between $150^\circ\text{-}160^\circ$ S3 Longitude (introduced in
535 section 3). This emission lies in a region which during the 2007 HST observations [Nichols
536 et al., 2009] featured the poleward edge of the UV main oval.

537 In the AEQ, for the first observation we find a large number of carbon/sulfur events
538 between the Io footprint ($\sim 5.8R_J$) and both the UV main oval and $30R_J$ contour. For the
539 AEQ, we also find ion emission poleward of the $30R_J$ contour. This is unexpected, since
540 previous observations showed that the majority of ion emission originated in the hot spot

541 quadrant. Emission from carbon/sulphur in the AEQ is largely absent from the second
542 observation.

543 For the 500-800eV oxygen emission (Figure 7b), events are also concentrated into the
544 auroral zone. In the first observation, the events occur poleward of the $30R_J$ contour and
545 the main oval reference contour in both the HSQ and AEQ, while in the second observa-
546 tion the auroral events are almost solely concentrated into the hot spot. Comparing the
547 oxygen with the carbon/sulfur emission, we find that where there is some carbon/sulphur
548 emission closer to the polar edge of the $30R_J$ contour, the oxygen emission generally origi-
549 nates poleward of this carbon/sulphur dominated emission region and appears to be more
550 diffusely distributed across the entire polar region.

551 Figure 7c shows the 800-1500eV emission, dominated by solar photons, distributed
552 across the disk and not concentrated into the aurora, as expected. The hard X-rays
553 (figure 7d) cluster in two regions in parallel with the $30R_J$ contour in the first observation
554 and are less prevalent in the second.

555 Figure 8 shows carbon/sulfur and oxygen latitude-count plots: the change between
556 observations in carbon/sulfur emission is similar in both quadrants, while oxygen emission
557 stays almost constant in the HSQ, but changes by a factor of 3 in the AEQ. This differing
558 behaviour and mapping for carbon/sulfur emission and oxygen emission may suggest
559 different sources for each.

7. Local Time Variation: Noon-Binned Projections and Magnetosphere Mapping

560 The configuration of Jupiter's magnetosphere will evolve throughout the observations.
561 As Jupiter rotates, a specific S3 longitude-latitude auroral position will map to changing

562 magnetospheric local time sources. To identify how this rotation, and the associated
563 change in local time, changes the X-ray aurora and to identify possible magnetospheric
564 local time origins for features, we mapped the magnetosphere footprint configuration
565 at distinct sub-solar longitudes (SSL). The SSL indicates which Jovian S3 longitude is
566 directly facing the Sun at a given time - the location of noon.

567 To do this, we sub-divided each 11 hour observation into 50-minute time bins. For each
568 time bin, we compared the S3 coordinates of auroral spatial and spectral features with
569 their mapped source regions using the Jovian magnetosphere-ionosphere model from Vogt
570 et al. [2011].

571 The Vogt model maps contours of constant radial distance from the magnetic equator
572 to the ionosphere by ensuring that magnetic flux at the equator equals magnetic flux
573 in the ionosphere. This enabled us to map ionospheric footprints to their equatorial
574 magnetospheric origins up to $150 R_J$ from the planet, where the VIP4 model [Connerney
575 et al., 1998] used for previous Jupiter X-ray observations was limited to $30 R_J$ [Gladstone
576 et al., 2002; Elsner et al., 2005; Branduardi-Raymont et al., 2008]. The Vogt model
577 accounts for the bend-back of Jupiter's field lines, in order to map field lines to their
578 magnetospheric local time origins. For instance, this could inform us that a specific
579 ionospheric footprint maps to an equatorial magnetospheric source $50 R_J$ from the planet
580 at dawn magnetospheric local time.

581 Using NASA JPL Horizons ephemerides data, we chose the start and end times of 50
582 minute X-ray bins to coincide with 30° increments of SSL. X-rays emitted at times when
583 the SSL was $15^\circ - 45^\circ$ were compared to the Vogt et al. [2011] mapping model at SSL 30°
584 to identify the sources for these X-rays, and so on for each 30° SSL increment.

585 Joy et al. [2002] showed that the magnetopause location of Jupiter is bi-modal. During
586 periods of low solar wind dynamic pressure, the nose of the magnetopause standoff is
587 expected to reach $\sim 92R_J$ (an expanded magnetosphere), whilst for the high dynamic
588 pressure periods, it will be as close as $\sim 63R_J$ (a compressed magnetosphere). Vogt et al.
589 [2011] account for these two different possible magnetopause standoff distances by moving
590 the magnetopause location based on the measured distances of Joy et al. [2002].

591 The plotted projections in figures 9 – 11 show the expanded magnetosphere mapping
592 of Vogt et al. [2011]. The magnetopause is indicated by a thick purple contour. Jupiter's
593 closed magnetic field lines map to latitudes equatorward of the magnetopause mapping.
594 Towards noon (at the nose of the magnetopause), these closed field lines are shown as
595 contours from $15 R_J$ (red contour) to $95 R_J$ (green contour), in increments of $5 R_J$.
596 For the compressed magnetosphere (figure 12) closed field line contours at the nose of
597 the magnetosphere extend only as far as $65 R_J$ (yellow contour). In the Jovian tail we
598 mapped closed field contours up to $150 R_J$. X-ray emission that maps to closed contours is
599 likely to be produced by precipitating particles on closed field lines originating in Jupiter's
600 magnetosphere. X-ray emission that maps poleward of the magnetopause, to the region
601 absent of contours, is from precipitating particles that are more likely to be on open field
602 lines.

603 Since Jupiter was close to opposition, the SSL and sub-observer longitude were only
604 $\sim 6^\circ$ separated, so that the noon position on the planet was close to the centre of the
605 observed disk. This means that counts originating near the limb of the Chandra-facing
606 disk are easily identifiable on the time-binned projections and their larger uncertainties
607 can be accounted for in the context of the magnetic footprint at that moment.

608 Analysing the SSL-binned polar projections with Vogt mapping revealed previously
609 unreported relationships. Firstly, for both the expanded and compressed magnetospheres
610 we find emission that mapped to the open field lines and also emission that mapped to
611 the magnetosphere, suggesting that both could be sources for Jovian auroral X-rays. For
612 the expanded model (figures 10 and 11) the majority of the emission originated on the
613 magnetosphere side of the magnetopause, while for the compressed model (figure 12) the
614 majority of emission originated on open field lines.

615 This may be particularly noteworthy for the ICME arrival observation. During this
616 observation a compression may be expected to shift the magnetopause boundary from
617 $\sim 92R_J$ to $\sim 63R_J$ [Joy et al., 2002]. It is this region mapping to 60-90 R_J , across which
618 the magnetopause would be compressed, which contained the hot spot expansion during
619 the first observation and where we observed increased X-ray emission. The closeness of
620 the emission to the magnetopause, our spatial uncertainties and our uncertainty in the
621 choice of expanded or compressed magnetosphere inhibited us from precisely quantifying
622 the relative importance of a solar wind vs a magnetospheric origin. The Vogt et al. [2011]
623 models showed, however, that the majority of X-ray producing ions originate beyond 60
624 R_J .

625 Figures 10 and 11 also show, and particularly for the first observation, that emission
626 clusters along the open-closed field line boundary and seems to move with SSL, suggesting
627 a local time dependence and relationship with processes in this region. The emission seems
628 to follow the region where field lines would be opening or where closed field lines occur in
629 the afternoon to dusk flank.

7.1. Noon-Binned Hot Spot Projections

630 For our observations, we considered the Hot Spot to be above 60° latitude and between
631 S3 longitudes 150° - 180° . We found for both observations that the hot spot had a strong
632 local time dependence and emitted 78 of 100 X-rays (first observation) and 51 of 74 X-
633 rays (second observation) before noon (165° SSL). After this time the Hot Spot became
634 dimmer, despite the region remaining observable on the Jovian disk for several hours after
635 this. Looking at the development of the magnetic field leading up to 165° SSL (figure
636 13), we found that the majority of the hot spot emission originated on the day-side of
637 Jupiter, with magnetospheric local times (MLT) between 10:30 and 18:00. Later in the
638 observation, when the field lines that mapped to MLTs after 18:00 were still observable
639 in the hot spot, we found significantly less emission from the region.

640 Having found that the Hot Spot emission occurred predominantly in the projections
641 90° - 150° SSL (figure 10 and 11) (prior to mapping to MLTs of 18:00), we analysed these
642 more closely. For the 90° SSL projection, the Hot Spot was close to the limb of the disk,
643 so there was a large uncertainty of 10° - 20° in the X-ray coordinates. Based on this, we
644 focused our attention on projections of 120° and 150° SSL (figures 12 and 13), where the
645 uncertainty was closer to 5° latitude-longitude.

646 Considering the first observation 120° SSL projection (figure 12 and 13), in the region
647 of 150° - 170° longitude and 55° - 80° latitude, carbon or sulfur (red) emission and oxygen
648 (blue) emission occurred along the field line contours. For the compressed magnetosphere,
649 both carbon/sulfur and oxygen ions originated along the open edge of the open-closed field
650 line boundary, while for the expanded magnetosphere the carbon/sulfur ions originated on
651 closed field lines. Accounting for spatial uncertainties, the carbon/sulfur events originated

652 between 50-90 R_J (yellow-green contours) and on open field lines, while the oxygen ions
653 originated poleward of this between 70-120 R_J (green contours) and also on open field
654 lines. The emission was weaker in the second observation for this SSL projection (figure
655 13).

656 For the 150° SSL projection, both observations (figure 13) contained clustering of X-
657 rays between 160-170° S3 longitude and 60-70° latitude from the afternoon-dusk flank of
658 the magnetosphere [Vogt et al., 2011]. Given that the time-binning is broad (50 minutes)
659 across 30° SSL, it is uncertain whether these field lines were open or closed for most of
660 this X-ray emission. Considering uncertainties in the spatial location, this region would
661 map either to the solar wind or closed field lines between 90-150 R_J . The similar source
662 in both 120° and 150° SSL may suggest that the processes are persistent.

663 Finally, inspecting the 210° SSL projection (figure 13), we found that the Hot Spot
664 contained very little emission, despite remaining on the observable disk. The emission
665 appeared to have followed those field lines that mapped to MLT regions from 12:00-18:00
666 as Jupiter rotated and we found emission in both the outer magnetosphere and on open
667 field lines in this area.

668 To reflect our spatial uncertainties, the timing spread of events and their broad spatial
669 distribution in each region, we found a broad range of MLT sources for the emission. For
670 the 120° and 150° SSL projection, most ion emission originated from magnetosphere loca-
671 tions with local times between 10:30-18:00. For the 210° SSL projection, events mapped
672 to MLTs of 8:30-19:00 (figure 13). However, we note that none of these MLTs account for
673 ion travel time from regions near the magnetopause to Jupiter's pole. During this time,
674 the magnetosphere will rotate and so the origins for the particles may be at earlier MLTs

675 than we have suggested. Without knowing the location of the energization region for the
676 ions, it is difficult to quantify this time lag.

7.2. Noon-Binned Auroral Enhancement Projections

677 To identify the source/s and development of the auroral enhancement we focus on the
678 240°, 270° and 300° SSL projections (figure 14). Unfortunately, the auroral region had just
679 begun to rotate out of view at this time, so a lot of the brightening occurred close to the
680 limb of the disk, meaning that there were uncertainties of 10°-20° on the S3 coordinates
681 of many X-rays.

682 The 270° SSL projection, when the auroral enhancement occurred, contained a broad
683 spread of emission from closed lines in the outer magnetosphere and field lines that were
684 open to the solar wind. This showed both oxygen and carbon/sulfur emission from the
685 open field line region. The emission broadly mapped across the dayside of the planet
686 between 06:00 to 16:00 MLT.

687 The 300° SSL projection had almost all the emission close to the limb, making it chal-
688 lenging to determine the location of the events because of the S3 uncertainties. Car-
689 bon/sulfur and oxygen emission appeared to originate from the magnetosphere, from
690 lower latitude regions than the 15 R_J footprint and from the open regions.

691 While we cautiously note that the counts were much lower for the hard X-ray emission
692 from electrons (green), the hard X-rays appeared to cluster on the dawn side of the disk.
693 This can be seen on the polar projections for SSLs 120°, 210° and 240° (figures 13 and
694 14). These regions mapped to MLTs 02:00-06:30hours. This is on the opposite side of the
695 magnetosphere to the origin for the precipitating ions, but is consistent with the vertex-

696 early dawn origin for the non-Io decametric emission that is observed coincident with the
697 first observation and which is also produced by electrons.

8. Timing Variation and Periodicity

698 Following the lead of Gladstone et al. [2002] and Elsner et al. [2005], we searched the
699 observations for periodicities by selecting a circle (Radius: 6.5° , Centre: 67° latitude,
700 170° longitude - see supporting information for further details) in S3 coordinates centred
701 on the hot spot and then fourier transformed the lightcurve from this region to generate
702 power spectral density (PSD) plots. We found that the area used by Gladstone et al.
703 [2002] and Elsner et al. [2005] showed periodicity at two significant timescales during our
704 first observation, at 12 and 26 minutes. Their significance increased by expanding the
705 circle to a radius of 8° , centred on 65° latitude and 163° S3 longitude. This larger region
706 included more of the broad spatial spread of hot spot emission in the first observation,
707 showing that the period was also present in the emission between the hot spot and 50
708 R_J contour. For the second observation, we found that the most statistically significant
709 period occurred using the same S3 circle as Gladstone et al. [2002] and Elsner et al. [2005].

710 To estimate the single-frequency probability of chance occurrence (PCO) for the de-
711 tected periods, we used the statistical methods of Leahy et al [1983]. The results are
712 shown as dotted horizontal lines on figures 15a, 15b, 15c and 15d. The lowest statistical
713 significance and therefore highest PCO of 10^{-1} is at the bottom of the plot and the highest
714 statistical significance and therefore lowest PCO of 10^{-6} is towards the top of the plot.

715 For the first observation, we found two strong periods (figure 15a). The most prominent
716 period occurred with a period of 26 minutes and a PCO of less than 10^{-6} . This is shorter
717 and more significant than the Gladstone et al. [2002] period (~ 45 min, 4×10^{-6}). The

718 second period had a timescale of 12 minutes and a PCO of 10^{-5} . We tested a range of
719 locations and sizes of regions encompassing the hot spot and found that these two periods
720 dominated, although which of the peaks was most dominant did swap. The 26 minute
721 peak was more dominant on the edge of the hot spot, where the carbon/sulfur particles
722 were more concentrated than oxygen. The 12 minute period was more dominant above
723 70° latitude where the carbon/sulfur and oxygen is more evenly distributed.

724 Periodicities in the second observation were weaker than in the first (figure 15b). The
725 most prominent period was at 42 minutes, with a PCO of 5×10^{-4} , not as significant as
726 the period in the first observation or that reported by Gladstone et al. [2002]. There was
727 also indication of a shorter period of 19 minutes, but this was even lower in significance.

728 To determine whether one period was associated with one particle population, we used
729 the same 8° radius region centred on 65° latitude and 163° S3 longitude and generated
730 PSDs for discrete energy ranges. Figure 15c shows a prominent 26 minute period at high
731 significance for the carbon/sulfur ions, with a PCO of 10^{-5} . It also shows a much weaker
732 12 minute period with a PCO of 2×10^{-3} . Conversely, the oxygen emission (figure 15d)
733 exhibited no 26 minute period and the strongest period was at 12 minutes with a PCO
734 of 5×10^{-3} . This suggests that one dominant sulfur/carbon population produced the 26
735 minute period, while a second combined population of sulfur/carbon and oxygen generated
736 the 12 minute period. For the second observation, the number of X-ray events was too
737 low to provide reliable results when separating the carbon/sulfur and oxygen populations.
738 The paucity of hard X-rays from precipitating electrons also made it difficult to identify a
739 significant period for them, although there is a suggestion of some 5-10 minute periodicity
740 for the first observation (see supporting information). We also tested regions across the

741 rest of the auroral zone and disk and found no other significant periods (see supporting
742 information).

743 The two periods in the first observation could have been due to harmonics, although in
744 this case it is challenging to explain how the period is divided between the two separate
745 particle populations in this manner. This division by energy also suggests that they are
746 unlikely to be from instrumental influence.

9. Summary of Results

747 We summarise results separately for the hot spot quadrant (S3 longitude: 90-180°) and
748 the auroral enhancement quadrant (S3 longitude: 180-270°), since solar wind conditions
749 may have been different for each (see figure 1) and the spatial, spectral and temporal
750 features differ.

751

9.1. Hot Spot Quadrant

752 • Spatial Emission: The change in emission in the hot spot is not as significant as in the
753 AEQ (Figure 4). This increased emission is concentrated between the previously reported
754 hot spot location [Gladstone et al., 2002; Elsner et al., 2005] and the 50 R_J footprint.
755 This gives the appearance of the hot spot having expanded for the first observation.

756 • Spectra: Both observations feature prominent 200-400 eV carbon/sulfur peaks and
757 a prominent peak in the OVII spectral region between 550-620 eV. The first observation
758 features either increased OVIII emission or increased solar photon emission.

759

760 • Energy Binned Polar Projections (figure 7): The 200-500 eV (carbon/sulfur) emis-
761 sion is mostly responsible for the increased emission between the normal hot spot location
762 and the 50 R_J footprint in the first observation. Generally, 500-800 eV (oxygen) emis-
763 sion occurs poleward of this concentrated carbon/sulfur emission. We also find that the
764 carbon/sulfur emission does not behave like the oxygen emission, with the carbon/sulfur
765 emission brightness more enhanced than the oxygen emission for this expanded hot spot.

766
767 • SSL projections with Vogt et al. [2011] model mapping: 78% (first observation) and
768 69% (second observation) of hot spot emission occurs before noon in the region. This
769 timing coincides with the region mapping to magnetospheric local times between 10:30-
770 18:00 hours. Most of the carbon/sulfur emission originates in the outer magnetosphere
771 between 50-90 R_J and on open field lines, while the oxygen emission originates further
772 from Jupiter (70-120 R_J) or on open field lines (with identification of an open or closed
773 origin depending on uncertainties in spatial resolution and choice of compressed/expanded
774 magnetosphere mapping). The expansion of the hot spot occurs on field lines mapping
775 to the region where the magnetopause has been found to move during compression from
776 92 R_J to 63 R_J [Joy et al., 2002]. The Vogt et al. [2011] model mapping showed that the
777 majority of X-ray producing ions originate beyond 60 R_J .

778
779 • PSDs: The first observation features 2 significant periods at 12 and 26 minutes -
780 shorter timescales than previously reported [Gladstone et al., 2002]. The second obser-
781 vation shows a less significant period of 42 minutes, closer to the 45 minute timescale
782 of Gladstone et al. [2002]. The 26 minute period is strong in carbon/sulfur emission

783 in the hot spot, but not in oxygen emission. The 12 minute period is present for both
784 carbon/sulfur and oxygen, but with much lower significance for each. When the two pop-
785 ulations are combined the period becomes significant.

786

9.2. Auroral Enhancement Quadrant

787 • Lightcurves: An auroral enhancement occurs during the first observation, the peak of
788 which is ~ 8 times brighter than for emission in the region during the second observation.
789 This occurs 1-1.5 hours before a non-Io decametric radio burst, a previously recognised
790 signature of ICME-induced forward shocks [Hess et al., 2012, 2014; Lamy et al., 2012].

791

792 • Spectra: The spectra from the first and second observation are different: there is an
793 enhanced 200-400 eV carbon/sulfur double peak and a prominent peak in the OVII spec-
794 tral region between 550-620 eV during the first observation. These peaks are much less
795 prominent in the second observation. Between 380-700 eV the spectrum appears similar
796 to cometary spectra from solar wind charge exchange [Elsner et al., 2005].

797

798 • Energy Binned Polar Projections: Both the 200-500eV (carbon/sulfur) and 500-
799 800eV (oxygen) emission is increased by a factor of at least 4 for both energy ranges in
800 the first observation relative to the second. This is different to the hot spot emission,
801 where carbon/sulfur is preferentially enhanced.

802

803 • SSL projections with Vogt et al. [2011] model mapping: The enhancements broadly
804 map across the dayside of the planet between 06:00 to 16:00 MLT parallel with the open-

805 closed boundary. The emission maps to open field lines and closed field lines in the outer
806 magnetosphere and also to low latitude regions between Io's footprint and the $15 R_J$ con-
807 tour.

808
809 • Hard X-rays: The 1500-5000 eV (electron bremsstrahlung) emission is observed in
810 clusters in the main oval region. It coincides with dawn on the surface and originates at
811 MLT 02:00-06:30 hours. This is on the opposite side of the magnetosphere to the source
812 of the X-ray charge exchanging ions.

813 • PSDs: No significant periodicity was detected from the AEQ ion emission.
814

10. Discussion

815 In the discussion, we attempt to address two questions: What are the source regions for
816 Jupiter's X-ray aurora? What processes in these regions produce X-rays and how might
817 these relate to the ICME?

818 The spectral, spatial and temporal differences between the hot spot and the auroral
819 enhancement emission lead us to treat the two features separately. Our analysis of the
820 periodicity, spectral and spatial origins of the emission suggests that both the hot spot
821 and auroral enhancement each have multiple X-ray sources regions.

822 Throughout the first observation, the SSL-binned projections with Vogt et al. [2011]
823 mapping show clustering of ion precipitation in the open field line region (figure 10). This
824 appears to indicate that there is at least some level of precipitation of ions from both
825 the open and closed field lines throughout the first observation. This is less clear for

826 the second observation, where there appears to be lower levels of open field line emission
827 and more is instead concentrated on closed field lines. The Vogt et al. [2011] models
828 showed that the majority of X-ray producing ions originate beyond $60 R_J$. If we assume a
829 compressed magnetosphere (with a stand-off distance at $63 R_J$ [Joy et al., 2002]), the open
830 field lines therefore contribute a large proportion of the emission, while for an expanded
831 magnetosphere (with a stand-off distance at $92 R_J$ [Joy et al., 2002]), closed field lines are
832 the dominant source.

10.1. The X-ray Hot Spot

833 10.1.1. Where is the Hot Spot Source?

834 While the auroral enhancement emission appeared to originate from several regions
835 that map to different magnetospheric locations, the hot spot remained confined to a more
836 limited region fixed in the planet's rotating frame. This spatial confinement permits more
837 precise identification of possible sources for the precipitating ions that produce X-ray
838 emission in this region.

839 The 200-500 eV sulfur and/or carbon emission features an additional component from
840 lower latitudes than the 500-800 eV oxygen emission. If we assume an expanded mag-
841 netosphere, we find that most of the 200-500 eV emission maps to a region between the
842 outer magnetosphere and the magnetopause, originating between 50 - $90 R_J$ (figure 12).
843 This model suggests that most 200-500 eV emission is from precipitation of high charge
844 state sulfur ions in the outer magnetosphere, as proposed by Cravens et al. [2003]. It also
845 suggests that there may be some slight precipitation from open field lines and therefore
846 possibly from carbon ions in the solar wind, but that this is a smaller proportion of the
847 emission. However, in the case of a compressed magnetosphere, the emission originates is

848 more evenly distributed between carbon ions in the solar wind and from sulfur ions from
849 the outer edge of the magnetosphere (for a compressed magnetosphere this is 50-63 R_J at
850 the stand-off point).

851 The observed strong 26 minute periodicity for these 200-500 eV X-rays may support
852 a sulfur source, since if the period originated in the solar wind we would expect to also
853 observe oxygen exhibiting it (as the most abundant heavy ion in the solar wind). The ab-
854 sence of oxygen emission from the 26 minute period and spatial separation between these
855 two species suggests that the lower latitude feature is from a dominant sulfur population,
856 which does not include oxygen of a sufficiently high charge state. The 12 minute period
857 increases in significance when oxygen is combined with carbon/sulfur, suggesting that
858 there is a second population consisting of a mixture of both oxygen and carbon/sulfur.
859 Alongside the periodicity, the spatial mapping suggests a different origin for each popula-
860 tion: one solely sulfur population with 26 minute periodicity from 50-70 R_J ; the other an
861 oxygen + carbon/sulfur population from closer to the magnetopause and possibly from
862 open field lines. Comparison of the two observations would seem to suggest that the
863 lower latitude sulfur dominated population is more sensitive to changes in the solar wind
864 conditions, since it is much more prevalent in the first observation.

865 Io injects both oxygen and sulfur into the Jovian magnetosphere, so if both X-ray-
866 producing populations originate in the outer magnetosphere, there needs to be an ex-
867 planation for why the 50-70 R_J region is dominated by sulfur emission and features less
868 oxygen emission. Oxygen ions that produce X-rays have a higher ionisation energy than
869 sulfur ions. For instance, O^{6+} requires 739 eV to become ionised [Drake, 1988], while
870 S^{6+} - S^{9+} only requires 281 - 447 eV [Biémont et al., 1999]. This means that it is possible

871 to have a magnetospheric region where there is sufficient energy for charge stripping and
872 X-ray production from sulfur, but not from oxygen. More energy would be expected to
873 be injected closer to the magnetopause either through pulsed dayside reconnection, where
874 the field lines closer to the magnetopause would be more perturbed [Bunce et al., 2004], or
875 through field aligned potentials [Cravens et al., 2003], which would be expected to increase
876 with radial distance from Jupiter. It is therefore possible, that either of these mechanisms
877 could create a higher energy region closer to the magnetopause and a lower energy region
878 deeper into the magnetosphere. It is also possible that quenching and opacity effects, as
879 suggested by Kharchenko et al. [2008] and Ozak et al. [2010], may need to be considered
880 to explain the spatial and periodic differences between the two populations.

881 Figure 16 summarises the equatorial mapping of the sources for different precipitating
882 particles generating the observed X-rays. Findings from recent work by Kimura et al.
883 [in prep] also identify similar sources for X-rays and identify both closed field lines in
884 the outer magnetosphere and open field lines beyond the magnetopause as possible X-ray
885 sources.

886 The presence of both magnetospheric and cusp precipitation is not precluded by the
887 findings of Cravens et al. [2003], Bunce et al. [2004] or Kharchenko et al. [2006, 2008],
888 but cusp precipitation would only be the dominant source of emission during auroral UV
889 flare-like conditions or heightened solar wind conditions. The mSWiM propagation and
890 radio emission shows solar wind densities increased at Jupiter during the first observation,
891 suggesting that these heightened solar wind conditions may have been present. Cusp
892 precipitation would include precipitation from protons, which are highly abundant in the
893 solar wind and would be expected to generate bright polar UV flares [Cravens et al., 2003].

894 Without coincident UV observations at the time of the X-ray observations reported here,
895 it is difficult to identify levels of proton precipitation and therefore to further separate
896 a solar wind or magnetosphere source for the higher latitude mixed population of high
897 charge-state oxygen and carbon/sulphur.

898 The precise magnetospheric origins of each particle depends on not only the spatial
899 uncertainties but also the internal field model used to initialise the Vogt et al. [2011]
900 mapping. Vogt et al. [2015] analyses the differences in each model (VIP4 [Connerney
901 et al., 1998], Grodent Anomaly Model[Grodent et al., 2008] and VIP Anomaly Longitude
902 [Hess et al., 2011]) and highlights the differences between each. From a simple X-ray
903 Hot Spot comparison, we found that the Grodent Anomaly Model we used in this work
904 normally mapped X-rays closer to Jupiter. VIPAL and VIP4 often mapped emission
905 beyond the magnetopause. When the Grodent Anomaly Model did map X-rays more
906 distantly than VIP4, then there was often less than a $10 R_J$ separation and local times
907 were often 0.5-3 hours later than VIP4 or VIPAL.

908 **10.1.2. What Process Drives the Hot Spot X-ray Emission?**

909 We find that in both observations the ions that precipitate to produce the hot spot
910 originate from locations between 10:30-18:30 on the dayside magnetosphere. Particularly,
911 we find that emission occurs alongside locations where recently opened field lines may
912 occur or on closed field lines in the afternoon flank (but still close to the magnetopause
913 and on the dayside of the planet). Bonfond et al. [2011] map quasi-periodic auroral flares
914 in the Far UV to the same region in Jupiter's magnetosphere at local times between 10:00
915 and 18:00 and note the similarity between these flares and flux transfer events observed

916 by Pioneer and Voyager probes. They suggest possible connections between these UV and
917 X-ray features and the Jovian cusp.

918 Combined with the dayside origin, the periodicities observed may also be a clue to
919 the mechanisms driving the emission. Using Ulysses, Marhavilas et al. [2001] found dual
920 periods of 15 - 20 minutes and 40 minutes in energetic particles upstream from the Jo-
921 vian bow shock. This may indicate a solar wind connection for emission. Ulysses also
922 detected 20 minute and 40 minute periodicities in the dusk magnetosphere [Anagnos-
923 topoulos et al., 1998, 2001; Karanikola et al., 2004]. Alternatively, the 12 minute period
924 falls within the 10-20 minute timescale of Jovian global ultra-low-frequency oscillations
925 [Khurana and Kivelson, 1989]. High energy ions have also been previously observed to
926 have periods within this range [Wilson and Dougherty, 2000]. At Earth, Ultra Low Fre-
927 quency waves are often associated with: dayside reconnection [Prikryl et al., 1998] or
928 with either compression from shock events or Kelvin Helmholtz instabilities [Dungey and
929 Loughhead, 1954; Chandrasekhar, 1961; Kivelson and Russell, 1995]. It seems possible
930 that one or more of these mechanisms may contribute to the detected hot spot periods in
931 our observations.

932 Bunce et al. [2004] found that pulsed dayside reconnection perturbing outer magne-
933 tosphere field lines would generate arc-like emission and a \sim 30-50 minute period, not
934 dissimilar to the 26 minute period we observe. They also suggest that this is more likely
935 to occur during high solar wind pressure, such as during our first observation. At this
936 time, in support of a reconnection origin, emission appears to cluster close to regions
937 where reconnection could occur (figure 10). Desroche et al. [2012] found that reconec-
938 tion was possible in the afternoon to dusk region based on plasma flow shear speeds,

939 $\beta=10$ and $\beta=1$, which may suggest the local time dependence of hot spot emission could
940 be connected with this process.

941 If the 26 minute periodicity were to be related to bounce times on field aligned po-
942 tentials instead, then it remains challenging to explain the shared 12 minute oxygen and
943 carbon/sulfur period in this way. This is because the different masses of oxygen and
944 sulfur/carbon would produce different bounce times for ions that originated in the same
945 region. Their shared period may therefore favour a non-bounce time related mechanism
946 for the 12 minute period in the first observation. We note that this 12 minute period
947 is of the same order of magnitude as the Alfvén wave transit times calculated by Bunce
948 et al. [2004]. If the periodicity does relate to the Alfvén transit time, then the shift in
949 period from 12 or 26 minutes to 42 minutes may make sense in the context of a shift
950 in magnetopause distance because of solar wind induced compression/expansion of the
951 magnetosphere.

952 For the second observation, when the solar wind was returning to pre-ICME condi-
953 tions, emission still originates from the dayside of the planet but more prominently from
954 locations in the magnetosphere closer to 15:00-18:00 MLT, along recently closed field
955 lines (figure 13). Kimura et al. [in prep.] suggest that flow shear effects such as Kelvin
956 Helmholtz instabilities (KHIs), also found at the magnetopauses of Saturn [Masters et al.,
957 2010; Wilson et al., 2012] and Earth [Hasegawa et al., 2004], may be an important fac-
958 tor, and thus an explanation for the periodicity in the Jovian X-ray emission. KHIs are
959 expected to develop on both the dawn and dusk flanks of the planet and are expected to
960 become more substantial moving down the flanks, where the velocity shears are larger,
961 as the magnetosphere and solar wind become progressively more rolled-up [Miura, 1984;

962 Nykyri et al., 2006]. These structures could either inject solar wind particles directly into
963 the magnetosphere, through small scale reconnection events [Fairfield et al., 2000; Nykyri
964 and Otto, 2001] or could facilitate the transport of momentum across the magnetopause
965 boundary layer [Miura, 1984; Chen and Kivelson, 1993], during the linear- phase prior
966 to roll-up. Multiple current systems are generated by KHIs [Masters et al., 2010], which
967 may provide the needed energisation source to create the high charge-state ions that can
968 produce X-rays.

969 At Earth, Taylor et al. [2012] reported a dawn-dusk asymmetry in rolled-up vortices
970 detection, with higher frequency on the post-noon dusk flank, while a previous study by
971 Hasegawa et al. [2006] reported as many KHIs on either flank. Unlike Earth, the Jovian
972 magnetosphere is populated by highly co-rotating plasma [Thomsen et al., 2010; Mauk
973 et al., 2009], which contributes to a larger shear at the dawnside, where the corotation
974 is sunward [Johnson et al., 2014]. As a result, this larger shear is expected to favour
975 the generation of KHI on the dawnside rather than on the duskside [Desroche et al.,
976 2012, 2013]. However, based on the development timescale of KH vortices in relevance to
977 Jovian orbital period, the structures at the dawn and dusk flanks may primarily originate
978 from the same location [Johnson et al., 2014], which could result in observation of rolled-up
979 vortices at earlier MLTs.

980 KHIs similar to those at Earth are less able to explain the first observation emission that
981 originates closer to the nose of the magnetosphere, near to noon MLT. Cowley et al. [2007],
982 however, find that flow shear along the open-closed field line boundary would be important
983 at Jupiter and capable of generating high latitude aurora. The shear increases when the
984 magnetosphere is compressed due to increased angular velocity of the magnetospheric

985 plasma, which could cause auroral emission to brighten [Nichols et al., 2009], so it may
986 be that flow shear is also relevant close to the nose.

987 It remains unclear as to why the hot spot feature is localised in these and previous
988 observations [Elsner et al., 2005; Gladstone et al., 2002; Branduardi-Raymont et al., 2008]
989 and restricted to limited longitudes of the Jovian pole. If the hot spot is driven by KHIs
990 or dayside reconnection, then this may imply either that these processes are localised for
991 the Jovian magnetosphere or that the high energy downward current region that produces
992 X-rays is localised.

993 The high energy electrons that generate the bremsstrahlung emission originate on the
994 opposite side of the planet to the ion emission, in regions between 02:00-06:30 magneto-
995 spheric local time. At Earth, similar features are associated with whistler mode waves
996 and the dawn chorus. The possible periodicity in the 5 - 10 minute range may be con-
997 sistent with this explanation. Dawn storms at Jupiter have been observed in the UV on
998 several prior occasions [e.g: Gustin et al. [2006]; Clarke et al. [2009]; Nichols et al. [2009]]
999 and may be capable of supplying sufficiently energetic electrons for X-ray brehmstrahlung
1000 emission. The hard X-ray emission from high energy electron precipitation also increased
1001 during the first observation. Brightening of the UV main emission has been observed to
1002 occur coincident with solar wind shocks [e.g:Nichols et al. [2009]]. Simultaneous UV-X-ray
1003 observations would help to further constrain these connections between brightness varia-
1004 tion in the UV main oval and increased hard X-ray emission from high energy electrons in
1005 this region. They would also help to identify global current systems, with UV helping to
1006 highlight upward currents (away from the planet) and X-rays from ions helping to identify
1007 downward currents (towards the planet).

10.2. The Auroral Enhancement

10.2.1. Where is the Auroral Enhancement Source?

1008
1009 In the quadrant from 180° - 270° S3 longitude, we note the largest change in auroral
1010 emission between the two observations the bright auroral enhancement on Day of Year
1011 276.25. The brightest peak of this event lasts ~ 20 minutes, 2-4 times longer than the flare
1012 reported by Elsner et al. [2005].

1013 Figures 7 and 14 show that the ion emission originates from a range of different latitudes
1014 and therefore maps to several different closed and open field line regions, suggesting that,
1015 at this time, there may be several downward current regions on which the ions can precip-
1016 itate. The precipitating particles also originate from a range of different magnetospheric
1017 local times across the dayside of Jupiter from dawn to close to dusk.

10.2.2. What Process Connected to the ICME Drives the Observed Auroral Enhancement?

1020 The auroral enhancement occurs 1-1.5 hours prior to a bright non-Io decametric radio
1021 burst (figure 2), which has previously been found to relate to the impingement of a solar
1022 wind forward shock [Gurnett et al., 2002; Lamy et al., 2012; Hess et al., 2012, 2014].
1023 The mSWiM propagation also suggests the arrival of an ICME close to this time. The
1024 combination of this radio emission and the mSWiM predicted solar wind density peak
1025 leads us to believe that the bright X-ray auroral enhancement is driven directly by this
1026 ICME.

1027 What process could be directly responsible for this X-ray brightening? The driver does
1028 not seem to be a continuation of the same process that produces the hot spot emission
1029 because the properties of the two emissions differ. The prominent differences between the

1030 AEQ and HSQ emission include: a different population of precipitating particles (figures
1031 6 and 8); the enhancement emission is spatially less localised than the hot spot emission
1032 (figures 3, 7, 8, 10, 11, 12, 13 and 14); the enhancement emission seems to increase
1033 temporally into a concentrated flare-like event, with no significant periodicity in the ion
1034 emission (figures 5 and 15), while the hot spot emission exhibits clear pulsations.

1035 The AEQ features also seem atypical when compared with other X-ray observations
1036 [Elsner et al., 2005; Gladstone et al., 2002; Branduardi-Raymont et al., 2008]. While the
1037 hot spot may be driven by KHIs or pulses of dayside reconnection close to a downward
1038 current region, we suggest that the auroral enhancement is driven by a less common
1039 process that is directly associated with the changing solar wind parameters induced by
1040 the ICME. Inspecting the mSWiM propagation (Figure 1) implies that the driver relates to
1041 either increased solar wind density and/or changing Interplanetary Magnetic Field angle
1042 (as suggested by the rotation in B_T). We propose two possible drivers based on these
1043 changing solar wind parameters but note that they might not be independent drivers:
1044 1) an ICME-induced compression event or 2) an-ICME induced instance of large-scale
1045 dayside reconnection.

1046 Increased ram pressure from the heightened solar wind density (Figure 1a) could drive a
1047 Jovian magnetosphere compression. The Vogt et al. [2011] mapping shows X-ray emission
1048 from several regions inside the magnetosphere, suggesting that the ICME transfers energy
1049 into the magnetosphere, so that ions are sufficiently energetic for X-ray production. This
1050 also raises questions as to the location of the downward currents (on which the ions
1051 precipitate) at this time. Compression events have been suggested to drive changes in
1052 Jupiter's current system and therefore acceleration processes [Cowley et al. 2007; Cowley

1053 and Bunce 2003A; 2003B]. Adjustments to the location of downward currents, induced by
1054 the compression, may therefore explain the observed broad spatial spread of ion emission,
1055 which during the auroral enhancement is not restricted to the hot spot as it normally is.

1056 Alternatively, or in combination with a compression, a large-scale instance of dayside
1057 reconnection may explain the observations. Desroche et al. [2012] showed that dayside
1058 reconnection would be confined to local regions on the magnetopause for certain IMF
1059 orientations, but varying IMF angle could lead dayside reconnection to occur across a
1060 larger proportion of the magnetopause. Masters [2015] further shows for Saturn that
1061 changing IMF angle can lead to increased reconnection voltages and a larger spatial scale
1062 of magnetopause reconnection. This could result in increased injection of solar wind
1063 particles and energisation of a larger region of the outer magnetosphere plasma, explaining
1064 the observations of the larger spatial scale of emission and the observed change in the
1065 precipitating population from the spectra. The inverse of this mechanism may also help
1066 to explain reduced emission from the hot spot for some observations, since a less favourable
1067 IMF angle would suppress reconnection and therefore emission from the hot spot. Further
1068 comparison of Jupiter X-ray emission with upstream IMF measurements would help to
1069 investigate this relationship.

1070 The Vogt et al. [2011] mapping also lends weight to the argument that solar wind-
1071 magnetosphere coupling is at work during this interval. It is possible that the solar
1072 wind compression and/or possible associated dayside reconnection for favourable IMF
1073 direction can lead to an opening of magnetic flux on the dayside, and concurrent X-ray
1074 flaring. Cravens et al. [2003], addressing charge exchange, show that X-ray emissivity
1075 from solar wind particles depends on solar wind velocity and density, which is in-line with

1076 our observation of increased emission. We also found that the magnetospheric mapping
1077 suggests an open field line origin for at least some of the emission. This is supported
1078 by similarities between the AEQ spectrum and cometary spectra, which are known to be
1079 produced by solar wind charge exchange (from direct solar wind precipitation). However,
1080 we are cautious to note that the complex configuration of the Jovian magnetosphere at
1081 this time may not be accurately represented by the Vogt et al. [2011] mapping model, so
1082 the magnetospheric mapping at this time may be less reliable.

1083 The low frequency of such ICME events, relative to the timescales of X-ray observations,
1084 may help to explain why these features have not been previously reported in the literature
1085 and why the second observation seems to have an AEQ that is again largely devoid of
1086 emission. We also note that such events may be confused with hot spot emission, if they
1087 occur at a time when the hot spot is in the observable quadrant, as opposed to this
1088 observation where the hot spot was rotating out of view when the auroral enhancement
1089 occurred.

1090 While we suggest that the solar wind does drive several changes in Jupiter's X-ray
1091 aurora, we note that the importance of the solar wind as a driver of magnetospheric
1092 dynamics, and that the existence of Dungey cycle processes at Jupiter remains a subject
1093 of debate [McComas and Bagenal, 2007, 2008; Cowley et al., 2008].

1094 Given that our findings are based on only two observations with this type of analysis,
1095 application of this approach to other observations would help to determine whether these
1096 features persist, how and where they originate and whether there are systematic trends
1097 between the X-ray aurora and solar wind.

11. Conclusion

1098 We report the first X-ray observation that was planned to coincide with an ICME arrival
1099 at Jupiter and find evidence for ICME-induced changes in the Northern X-ray aurora. We
1100 observe changes in the morphology, spectra and periodicity of the emission at this time.
1101 We particularly find an auroral enhancement by a factor 8, occurring 1-1.5 hours before
1102 a bright burst of non-*Io* decametric radio emission, often associated with the arrival of
1103 an ICME-induced fast forward shock [Hess et al., 2012, 2014; Lamy et al., 2012] and at a
1104 time when solar wind propagation models indeed predict an ICME arrival.

1105 We have used Vogt et al. [2011] magnetospheric mapping to identify the origin of the
1106 X-ray emission. This mapping suggests that most auroral X-ray emission came from pre-
1107 cipitating ions with origins beyond 60 R_J on both open and closed field lines. Spatial
1108 uncertainties and uncertainties as to whether the magnetosphere is compressed or ex-
1109 panded at this time inhibit us from quantifying from which side of the magnetopause the
1110 majority of emission originates. The region between 50-70 R_J is dominated by 200-500
1111 eV emission, which we attribute to precipitating high charge-state magnetospheric sulfur
1112 ions. At higher latitudes that map between 70-120 R_J and to open field lines there is a
1113 mixture of precipitating high charge-state carbon/sulphur and oxygen ions.

1114 In the Hot Spot, these separate origins for ions of different species is supported by
1115 periodicity measurements. In the first observation we find a strong 26 minute period
1116 associated with the carbon/sulfur (200-500 eV) emission, but not with the oxygen (500-
1117 800 eV) emission. We do, however, find a 12 minute period at a low level of significance
1118 in both the oxygen and carbon/sulfur emission. When the two populations are combined,
1119 the 12 minute period becomes significant. The periods of 12 and 26 minutes in the first

1120 observation are distinctly shorter than the 42 minute period we detect in the second
1121 observation, which is close to the 45 minute timescale found by Gladstone et al. [2002].

1122 X-ray emission is concentrated in regions near to open field lines. On the basis of
1123 the magnetospheric local time of the source and the origin close to the magnetopause,
1124 alongside the periodicities and heightened solar wind conditions, we suggest that pulses
1125 of dayside reconnection [Bunce et al., 2004; Desroche et al., 2012] near a magnetospheric
1126 downward current region could be driving the X-ray hot spot emission. We also suggest
1127 that the spectral, spatial and temporal differences between the hot spot emission and
1128 auroral enhancement emission imply that they are not created by a continuation of the
1129 same process. Instead, we suggest that the auroral enhancement is directly driven by
1130 the ICME through either a compression event and/or a larger-scale instance of dayside
1131 reconnection than that producing the hot spot emission.

1132 Other mechanisms in the outer magnetosphere, near the magnetopause, such as KHIs,
1133 may also have an important role in transferring momentum and energy in our observations,
1134 given that the Dungey cycle may well be less important for Jupiter than Earth [McComas
1135 and Bagenal, 2007, 2008; Delamere and Bagenal, 2010; Johnson et al., 2014].

1136 We believe that the approach of applying Vogt et al. [2011] model mapping to energy-
1137 binned, sub-solar longitude-binned X-rays offers excellent possibilities for mapping the
1138 origins of the Jovian X-ray aurora and thus better understanding the Jovian outer mag-
1139 netosphere and the processes occurring close to the magnetopause. Similar analysis on
1140 new and archival X-ray observations is required to determine whether the features ob-
1141 served in these observations persist and how they relate to systematic trends in solar
1142 wind conditions. Combining observations of this kind with the approach and arrival of

1143 the Juno spacecraft in 2016 will offer further opportunities to understand the processes
1144 governing Jovian auroral X-rays.

1145 **Acknowledgments.** WRD is supported by an Science and Technology Facilities Coun-
1146 cil (STFC) studentship. RFE acknowledges support by NASA's Chandra Program PGF
1147 was supported by SAO subcontract SV3-73016 of NASA contract NAS8-03060. AJC
1148 acknowledges support via the UCL-MSSL consolidated grant, from STFC (UK). LL is
1149 supported by CNES. CMJ is supported by a Science and Technology Facilities Council
1150 Ernest Rutherford Fellowship. JDN was supported by an STFC Advanced Fellowship
1151 (ST/ I004084/1) IJR is funded in part by the UK Science and Technology Facilities
1152 Council (STFC) grant ST/L000563/1, and Natural and Environmental Research Council
1153 (NERC) grant NE/L007495/1 TK was supported by a grant-in-aid for Scientific Research
1154 from the Japan Society for the Promotion of Science (JSPS). We warmly thank R. Kraft,
1155 A. Masters and L. Ray for very helpful discussions. We also thank the anonymous ref-
1156 eree who expressed interest in searching for periodicity at hard X-rays, which led us to
1157 finding possible evidence for it. This work is mainly based on observations of the NASA
1158 Chandra X-ray Observatory (Observations 12315 and 12316). These observations are
1159 available from the Chandra Data Archive (<http://cda.harvard.edu/chaser/>). We thank
1160 the Chandra Project for their support. We also used data acquired by the SECCHI and
1161 WAVES experiments of the NASA STEREO spacecraft (available from: [http://stereo-](http://stereo-ssc.nascom.nasa.gov/data.shtml)
1162 ssc.nascom.nasa.gov/data.shtml) and by NASA's Solar X-ray Imager on the GOES space-
1163 craft (available from: <http://sxi.ngdc.noaa.gov/sxi/servlet/sxisearch>). We would like to
1164 thank these teams for their support. We would also like to thank both our reviewers for
1165 all their valuable insight and input.

References

- 1166 GC Anagnostopoulos, A Balogh, PK Marhavilas, AG Rigas, ET Sarris, and PC Trochout-
1167 sos. Quasi-periodic behavior of ion events and wave activity upstream from jupiter's
1168 bow shock: Ulysses' observations. *Geophysical research letters*, 25(9):1533–1536, 1998.
- 1169 GC Anagnostopoulos, I Karanikola, and P Marhavilas. Large-scale energetic particle
1170 layers in the high latitude jovian magnetosphere. *Planetary and Space Science*, 49(10):
1171 1049–1065, 2001.
- 1172 KA Arnaud. Xspec: The first ten years. In *Astronomical Data Analysis Software and*
1173 *Systems V*, volume 101, page 17, 1996.
- 1174 RL Baron, T Owen, JEP Connerney, T Satoh, and J Harrington. Solar wind control of
1175 jupiter's h+ 3 auroras. *Icarus*, 120(2):437–442, 1996.
- 1176 CH Barrow, F Genova, and MD Desch. Solar wind control of jupiter's decametric radio
1177 emission. *Astronomy and Astrophysics*, 165:244–250, 1986.
- 1178 Anil Bhardwaj, Graziella Branduardi-Raymont, Ronald F Elsner, G Randall Gladstone,
1179 Gavin Ramsay, Pedro Rodriguez, Roberto Soria, JH Waite, and Thomas E Cravens.
1180 Solar control on jupiter's equatorial x-ray emissions: 26–29 november 2003 xmm-newton
1181 observation. *Geophysical Research Letters*, 32(3), 2005.
- 1182 Anil Bhardwaj, Ronald F Elsner, G Randall Gladstone, J Hunter Waite, Graziella
1183 Branduardi-Raymont, Thomas E Cravens, and Peter G Ford. Low-to middle-latitude x-
1184 ray emission from jupiter. *Journal of Geophysical Research: Space Physics (1978–2012)*,
1185 111(A11), 2006.
- 1186 Emile Biémont, Y Frémat, and Pascal Quinet. Ionization potentials of atoms and ions
1187 from lithium to tin ($z= 50$). *Atomic Data and Nuclear Data Tables*, 71(1):117–146,

- 1188 1999.
- 1189 Bertrand Bonfond, MF Vogt, J-C Gérard, Denis Grodent, Aikaterini Radioti, and Valérie
1190 Coumans. Quasi-periodic polar flares at jupiter: A signature of pulsed dayside recon-
1191 nections? *Geophysical Research Letters*, 38(2), 2011.
- 1192 G Branduardi-Raymont, RF Elsner, GR Gladstone, G Ramsay, P Rodriguez, R Soria, and
1193 JH Waite Jr. First observation of jupiter by xmm-newton. *Astronomy & Astrophysics*,
1194 424(1):331–337, 2004.
- 1195 G Branduardi-Raymont, A Bhardwaj, RF Elsner, GR Gladstone, G Ramsay, P Rodriguez,
1196 R Soria, JH Waite, and TE Cravens. Latest results on jovian disk x-rays from xmm-
1197 newton. *Planetary and Space Science*, 55(9):1126–1134, 2007a.
- 1198 G Branduardi-Raymont, A Bhardwaj, RF Elsner, GR Gladstone, G Ramsay, P Rodriguez,
1199 R Soria, JH Waite, TE Cravens, et al. A study of jupiter’s aurorae with xmm-newton.
1200 *Astronomy & Astrophysics*, 463(2):761–774, 2007b.
- 1201 G Branduardi-Raymont, Ronald F Elsner, M Galand, Denis Grodent, TE Cravens, P Ford,
1202 GR Gladstone, and JH Waite. Spectral morphology of the x-ray emission from jupiter’s
1203 aurorae. *Journal of Geophysical Research: Space Physics (1978–2012)*, 113(A2), 2008.
- 1204 EJ Bunce, SWH Cowley, and TK Yeoman. Jovian cusp processes: Implications for the
1205 polar aurora. *Journal of Geophysical Research: Space Physics (1978–2012)*, 109(A9),
1206 2004.
- 1207 Subrahmanyan Chandrasekhar. *Hydrodynamic and Hydrodynamic stability*. OUP, 1961.
- 1208 S-H Chen and MG Kivelson. On nonsinusoidal waves at the earth? s magnetopause.
1209 *Geophysical research letters*, 20(23):2699–2702, 1993.

- 1210 D Chua, G Parks, M Brittnacher, W Peria, G Germany, J Spann, and C Carlson. En-
1211 ergy characteristics of auroral electron precipitation: A comparison of substorms and
1212 pressure pulse related auroral activity. *Journal of Geophysical Research: Space Physics*
1213 *(1978–2012)*, 106(A4):5945–5956, 2001.
- 1214 JT Clarke, J Nichols, J-C Gérard, Denis Grodent, KC Hansen, William Kurth, GR Glad-
1215 stone, J Duval, S Wannawichian, E Bunce, et al. Response of jupiter’s and saturn’s
1216 auroral activity to the solar wind. *Journal of Geophysical Research: Space Physics*
1217 *(1978–2012)*, 114(A5), 2009.
- 1218 JEP Connerney, MH Acuna, NF Ness, and T Satoh. New models of jupiter’s magnetic
1219 field constrained by the io flux tube footprint. *Journal of Geophysical Research: Space*
1220 *Physics (1978–2012)*, 103(A6):11929–11939, 1998.
- 1221 SWH Cowley and EJ Bunce. Origin of the main auroral oval in jupiter’s coupled
1222 magnetosphere-ionosphere system. *Planetary and Space Science*, 49(10):1067–1088,
1223 2001.
- 1224 SWH Cowley and EJ Bunce. Modulation of Jovian middle magnetosphere currents and
1225 auroral precipitation by solar wind-induced compressions and expansions of the magne-
1226 tosphere: initial response and steady state. *Planetary and Space Science*, 51(1):31–56,
1227 2003.
- 1228 SWH Cowley and EJ Bunce. Modulation of Jupiter’s main auroral oval emissions by solar
1229 wind induced expansions and compressions of the magnetosphere *Planetary and Space*
1230 *Science*, 51(1):57–79, 2003.
- 1231 SWH Cowley, JD Nichols, and DJ Andrews. Modulation of jupiter’s plasma flow, polar
1232 currents, and auroral precipitation by solar wind-induced compressions and expansions

1233 of the magnetosphere: a simple theoretical model. In *Annales Geophysicae*, volume 25,
1234 pages 1433–1463, 2007.

1235 SWH Cowley, Sarah V Badman, SM Imber, and SE Milan. Comment on Jupiter: A fun-
1236 damentally different magnetospheric interaction with the solar wind? by DJ McComas
1237 and F. Bagenal. *Geophysical Research Letters*, 35(10), 2008.

1238 TE Cravens. Comet hyakutake x-ray source: Charge transfer of solar wind heavy ions.
1239 *Geophysical research letters*, 24(1):105–108, 1997.

1240 TE Cravens, E Howell, JH Waite, and GR Gladstone. Auroral oxygen precipitation at
1241 jupiter. *Journal of Geophysical Research: Space Physics (1978–2012)*, 100(A9):17153–
1242 17161, 1995.

1243 TE Cravens, JH Waite, TI Gombosi, N Lugaz, GR Gladstone, BH Mauk, and RJ Mac-
1244 Dowall. Implications of jovian x-ray emission for magnetosphere-ionosphere coupling.
1245 *Journal of Geophysical Research: Space Physics (1978–2012)*, 108(A12), 2003.

1246 TE Cravens, J Clark, A Bhardwaj, R Elsner, JH Waite, AN Maurellis, GR Gladstone, and
1247 G Branduardi-Raymont. X-ray emission from the outer planets: Albedo for scattering
1248 and fluorescence of solar x rays. *Journal of Geophysical Research: Space Physics (1978–*
1249 *2012)*, 111(A7), 2006.

1250 TE Cravens, and N Ozak. Auroral ion precipitation and acceleration at the outer planets.
1251 *Auroral Phenomenology and Magnetospheric Processes: Earth And Other Planets*, 287–
1252 294, 2012.

1253 PA Delamere and F Bagenal. Solar wind interaction with jupiter’s magnetosphere. *Journal*
1254 *of Geophysical Research: Space Physics (1978–2012)*, 115(A10), 2010.

- 1255 M Desroche, F Bagenal, PA Delamere, and N Erkaev. Conditions at the expanded jovian
1256 magnetopause and implications for the solar wind interaction. *Journal of Geophysical*
1257 *Research: Space Physics (1978–2012)*, 117(A7), 2012.
- 1258 M Desroche, F Bagenal, PA Delamere, and N Erkaev. Conditions at the magnetopause of
1259 saturn and implications for the solar wind interaction. *Journal of Geophysical Research:*
1260 *Space Physics*, 118(6):3087–3095, 2013.
- 1261 GW Drake. Theoretical energies for the $n=1$ and 2 states of the helium isoelectronic
1262 sequence up to $z=100$. *Canadian journal of physics*, 66(7):586–611, 1988.
- 1263 JW Dungey and RE Loughhead. Twisted magnetic fields in conducting fluids. *Australian*
1264 *Journal of Physics*, 7(1):5–13, 1954.
- 1265 E Echer, P Zarka, WD Gonzalez, A Morioka, and L Denis. Solar wind effects on jupiter
1266 non-io dam emissions during ulysses distant encounter (2003–2004). *Astronomy & As-*
1267 *trophysics*, 519:A84, 2010.
- 1268 RD Elphinstone, JS Murphree, and LL Cogger. What is a global auroral substorm?
1269 *Reviews of Geophysics*, 34(2):169–232, 1996.
- 1270 Ronald F Elsner, N Lugaz, JH Waite, TE Cravens, GR Gladstone, P Ford, Denis Grodent,
1271 A Bhardwaj, RJ MacDowall, MD Desch, et al. Simultaneous chandra x ray, hubble
1272 space telescope ultraviolet, and ulysses radio observations of jupiter’s aurora. *Journal*
1273 *of Geophysical Research: Space Physics (1978–2012)*, 110(A1), 2005.
- 1274 DH Fairfield, A Otto, T Mukai, S Kokubun, RP Lepping, JT Steinberg, AJ Lazarus, and
1275 T Yamamoto. Geotail observations of the kelvin-helmholtz instability at the equatorial
1276 magnetotail boundary for parallel northward fields. *Journal of Geophysical Research:*
1277 *Space Physics (1978–2012)*, 105(A9):21159–21173, 2000.

1278 J Geiss, G Gloeckler, H Balsiger, LA Fisk, AB Galvin, F Gliem, DC Hamilton,
1279 FM Ipavich, S Livi, U Mall, et al. Plasma composition in jupiter's magnetosphere:
1280 initial results from the solar wind ion composition spectrometer. *Science*, 257(5076):
1281 1535–1539, 1992.

1282 G Randall Gladstone, J Hunter Waite, and William S Lewis. Secular and local time
1283 dependence of jovian x ray emissions. *Journal of Geophysical Research: Planets (1991–*
1284 *2012)*, 103(E9):20083–20088, 1998.

1285 GR Gladstone, JH Waite, Denis Grodent, WS Lewis, FJ Crary, Ronald F Elsner,
1286 MC Weisskopf, T Majeed, J-M Jahn, A Bhardwaj, et al. A pulsating auroral x-ray
1287 hot spot on jupiter. *Nature*, 415(6875):1000–1003, 2002.

1288 Denis Grodent, JT Clarke, JH Waite, SWH Cowley, J-C Gérard, and J Kim. Jupiter's
1289 polar auroral emissions. *Journal of Geophysical Research: Space Physics (1978–2012)*,
1290 108(A10), 2003.

1291 Denis Grodent, Bertrand Bonfond, Jean-Claude Gérard, Aikaterini Radioti, Jacques
1292 Gustin, John T Clarke, Jonathan Nichols, and John EP Connerney. Auroral evidence of
1293 a localized magnetic anomaly in jupiter's northern hemisphere. *Journal of Geophysical*
1294 *Research: Space Physics (1978–2012)*, 113(A9), 2008.

1295 DA Gurnett, WS Kurth, GB Hospodarsky, AM Persoon, P Zarka, A Lecacheux,
1296 SJ Bolton, MD Desch, WM Farrell, ML Kaiser, et al. Control of jupiter's radio emission
1297 and aurorae by the solar wind. *Nature*, 415(6875):985–987, 2002.

1298 J. Gustin, S. W. H. Cowley, J.-C. Grard, G. R. Gladstone, D. Grodent, and J. T.
1299 Clarke. Characteristics of jovian morning bright fuv aurora from hubble space tele-
1300 scope/space telescope imaging spectrograph imaging and spectral observations. *Journal*

- 1301 of *Geophysical Research: Space Physics*, 111(A9):n/a–n/a, 2006. ISSN 2156-2202. doi:
1302 10.1029/2006JA011730. URL <http://dx.doi.org/10.1029/2006JA011730>. A09220.
- 1303 PG Hanlon, MK Dougherty, N Krupp, KC Hansen, FJ Crary, DT Young, and G Tóth.
1304 Dual spacecraft observations of a compression event within the jovian magnetosphere:
1305 Signatures of externally triggered supercorotation? *Journal of Geophysical Research:*
1306 *Space Physics (1978–2012)*, 109(A9), 2004.
- 1307 H Hasegawa, M Fujimoto, T-D Phan, H Reme, A Balogh, MW Dunlop, C Hashimoto, and
1308 R TanDokoro. Transport of solar wind into earth’s magnetosphere through rolled-up
1309 kelvin–helmholtz vortices. *Nature*, 430(7001):755–758, 2004.
- 1310 H Hasegawa, M Fujimoto, K Takagi, Y Saito, T Mukai, and H Rème. Single-spacecraft
1311 detection of rolled-up kelvin-helmholtz vortices at the flank magnetopause. *Journal of*
1312 *Geophysical Research: Space Physics (1978–2012)*, 111(A9), 2006.
- 1313 SLG Hess, Bertrand Bonfond, P Zarka, and Denis Grodent. Model of the jovian magnetic
1314 field topology constrained by the io auroral emissions. *Journal of Geophysical Research:*
1315 *Space Physics (1978–2012)*, 116(A5), 2011.
- 1316 SLG Hess, E Echer, and P Zarka. Solar wind pressure effects on jupiter decametric radio
1317 emissions independent of io. *Planetary and Space Science*, 70(1):114–125, 2012.
- 1318 SLG Hess, E Echer, P Zarka, L Lamy, and PA Delamere. Multi-instrument study of
1319 the jovian radio emissions triggered by solar wind shocks and inferred magnetospheric
1320 subcorotation rates. *Planetary and Space Science*, 99:136–148, 2014.
- 1321 TW Hill. The jovian auroral oval. *Journal of Geophysical Research: Space Physics (1978–*
1322 *2012)*, 106(A5):8101–8107, 2001.

- 1323 Yawei Hui, David R Schultz, Vasili A Kharchenko, Phillip C Stancil, Thomas E Cravens,
1324 Carey M Lisse, and Alexander Dalgarno. The ion-induced charge-exchange x-ray emis-
1325 sion of the jovian auroras: Magnetospheric or solar wind origin? *The Astrophysical*
1326 *Journal Letters*, 702(2):L158, 2009.
- 1327 Yawei Hui, David R Schultz, Vasili A Kharchenko, Anil Bhardwaj, Graziella Branduardi-
1328 Raymont, Phillip C Stancil, Thomas E Cravens, Carey M Lisse, and Alexander Dal-
1329 garno. Comparative analysis and variability of the jovian x-ray spectra detected by
1330 the chandra and xmm-newton observatories. *Journal of Geophysical Research: Space*
1331 *Physics (1978–2012)*, 115(A7), 2010.
- 1332 CM Jackman and CS Arridge. Solar cycle effects on the dynamics of Jupiter’s and Saturn’s
1333 magnetospheres *Solar Physics*, 274:1–2 481–502, 2011.
- 1334 Jay R Johnson, Simon Wing, and Peter A Delamere. Kelvin helmholtz instability in
1335 planetary magnetospheres. *Space Science Reviews*, 184(1-4):1–31, 2014.
- 1336 SP Joy, MG Kivelson, RJ Walker, KK Khurana, CT Russell, and T Ogino. Probabilistic
1337 models of the jovian magnetopause and bow shock locations. *Journal of Geophysical*
1338 *Research: Space Physics (1978–2012)*, 107(A10):SMP–17, 2002.
- 1339 ML Kaiser. Time-variable magnetospheric radio emissions from jupiter. *Journal of Geo-*
1340 *physical Research: Planets (1991–2012)*, 98(E10):18757–18765, 1993.
- 1341 I Karanikola, M Athanasiou, GC Anagnostopoulos, GP Pavlos, and P Preka-Papadema.
1342 Quasi-periodic emissions (15–80min) from the poles of jupiter as a principal source of the
1343 large-scale high-latitude magnetopause boundary layer of energetic particle. *Planetary*
1344 *and Space Science*, 52(5):543–559, 2004.

- 1345 V Kharchenko, A Dalgarno, DR Schultz, and PC Stancil. Ion emission spectra in the
1346 jovian x-ray aurora. *Geophysical research letters*, 33(11), 2006.
- 1347 V Kharchenko, Anil Bhardwaj, A Dalgarno, David Robert Schultz, and Phillip C Stancil.
1348 Modeling spectra of the north and south jovian x-ray auroras. *Journal of Geophysical*
1349 *Research: Space Physics (1978–2012)*, 113(A8), 2008.
- 1350 Krishan K Khurana and Margaret G Kivelson. Ultralow frequency mhd waves in jupiter's
1351 middle magnetosphere. *Journal of Geophysical Research: Space Physics (1978–2012)*,
1352 94(A5):5241–5254, 1989.
- 1353 T Kimura et al. Dynamics and source location of jupiter's high energy x-ray aurora
1354 investigated by chandra, xmm newton, and hisaki satellite. in prep.
- 1355 Margaret G Kivelson and Christopher T Russell. *Introduction to space physics*. Cambridge
1356 university press, 1995.
- 1357 HP Ladreiter and Y Leblanc. Jovian hectometric radiation-beaming, source extension,
1358 and solar wind control. *Astronomy and Astrophysics*, 226:297–310, 1989.
- 1359 L Lamy, R Prangé, KC Hansen, JT Clarke, P Zarka, B Cecconi, J Abouadarham, N André,
1360 G Branduardi-Raymont, R Gladstone, et al. Earth-based detection of uranus' aurorae.
1361 *Geophysical Research Letters*, 39(7), 2012.
- 1362 D. Leahy, W. Darbro, R. Elsner, M. Weisskopf, S. Kahn, P. Sutherland, J. Grindlay On
1363 searches for pulsed emission with application to four globular cluster X-ray sources-NGC
1364 1851, 6441, 6624, and 6712. *The Astrophysical Journal*, 266(160–170), 1983.
- 1365 PK Marhavilas, GC Anagnostopoulos, and ET Sarris. Periodic signals in ulysses? ener-
1366 getic particle events upstream and downstream from the jovian bow shock. *Planetary*
1367 *and Space Science*, 49(10):1031–1047, 2001.

- 1368 A. Masters, N. Achilleos, M. G. Kivelson, N. Sergis, M. K. Dougherty, M. F. Thom-
1369 sen, C. S. Arridge, S. M. Krimigis, H. J. McAndrews, S. J. Kanani, N. Krupp,
1370 and A. J. Coates. Cassini observations of a kelvin-helmholtz vortex in sat-
1371 urn's outer magnetosphere. *Journal of Geophysical Research: Space Physics*,
1372 115(A7):n/a–n/a, 2010. ISSN 2156-2202. doi: 10.1029/2010JA015351. URL
1373 <http://dx.doi.org/10.1029/2010JA015351>. A07225.
- 1374 A. Masters. The dayside reconnection voltage applied to Saturn's magnetosphere *Geo-*
1375 *physical Research Letters*, 42(8):2577–2585, 2015.
- 1376 BH Mauk, DC Hamilton, TW Hill, GB Hospodarsky, RE Johnson, C Paranicas, E Rous-
1377 sos, CT Russell, DE Shemansky, EC Sittler Jr, et al. Fundamental plasma processes
1378 in saturn's magnetosphere. In *Saturn from Cassini-Huygens*, pages 281–331. Springer,
1379 2009.
- 1380 Ahilleas N Maurellis, Thomas E Cravens, G Randall Gladstone, J Hunter Waite, and
1381 Loren W Acton. Jovian x-ray emission from solar x-ray scattering. *Geophysical research*
1382 *letters*, 27(9):1339–1342, 2000.
- 1383 DJ McComas and F Bagenal. Jupiter: A fundamentally different magnetospheric inter-
1384 action with the solar wind. *Geophysical Research Letters*, 34(20), 2007.
- 1385 DJ McComas and F Bagenal. Reply to comment by sw h cowley et al. on ?jupiter: a
1386 fundamentally different magnetospheric interaction with the solar wind? *Geophysical*
1387 *Research Letters*, 35(10), 2008.
- 1388 Albert E Metzger, David A Gilman, Joe L Luthey, Kevin C Hurley, Herbert W Schnopper,
1389 Frederick D Seward, and James D Sullivan. The detection of x rays from jupiter. *Journal*
1390 *of Geophysical Research: Space Physics (1978–2012)*, 88(A10):7731–7741, 1983.

- 1391 Akira Miura. Anomalous transport by magnetohydrodynamic kelvin-helmholtz instabili-
1392 ties in the solar wind-magnetosphere interaction. 1984.
- 1393 JD Nichols and SWH Cowley. Magnetosphere-ionosphere coupling currents in jupiter's
1394 middle magnetosphere: Effect of precipitation-induced enhancement of the ionospheric
1395 pedersen conductivity. In *Annales Geophysicae*, volume 22, pages 1799–1827, 2004.
- 1396 JD Nichols, EJ Bunce, John T Clarke, SWH Cowley, J-C Gérard, Denis Grodent, and
1397 Wayne R Pryor. Response of jupiter's uv auroras to interplanetary conditions as ob-
1398 served by the hubble space telescope during the cassini flyby campaign. *Journal of*
1399 *Geophysical Research: Space Physics (1978–2012)*, 112(A2), 2007.
- 1400 JD Nichols, JT Clarke, Jean-Claude Gérard, Denis Grodent, and KC Hansen. Variation
1401 of different components of jupiter's auroral emission. *Journal of Geophysical Research:*
1402 *Space Physics (1978–2012)*, 114(A6), 2009.
- 1403 Jonathan D Nichols. Magnetosphere-ionosphere coupling in jupiter's middle magneto-
1404 sphere: Computations including a self-consistent current sheet magnetic field model.
1405 *Journal of Geophysical Research: Space Physics (1978–2012)*, 116(A10), 2011.
- 1406 K Nykyri and A Otto. Plasma transport at the magnetospheric boundary due to recon-
1407 nection in kelvin-helmholtz vortices. *Geophys. Res. Lett*, 28(18):3565–3568, 2001.
- 1408 K Nykyri, A Otto, B Lavraud, C Mouikis, LM Kistler, A Balogh, and H Reme. Cluster
1409 observations of reconnection due to the kelvin-helmholtz instability at the dawnside
1410 magnetospheric flank. In *Annales Geophysicae*, volume 24, pages 2619–2643, 2006.
- 1411 N Ozak, TE Cravens, and DR Schultz. Auroral ion precipitation at jupiter: Predictions
1412 for juno. *Geophysical Research Letters*, 40(16):4144–4148, 2013.

- 1413 Nataly Ozak, David Robert Schultz, TE Cravens, V Kharchenko, and Y-W Hui. Auroral
1414 x-ray emission at jupiter: Depth effects. *Journal of Geophysical Research: Space Physics*
1415 (1978–2012), 115(A11), 2010.
- 1416 Laurent Pallier and Renée Prangé. More about the structure of the high latitude jovian
1417 aurorae. *Planetary and Space Science*, 49(10):1159–1173, 2001.
- 1418 R Prangé, P Zarka, GE Ballester, TA Livengood, L Denis, T Carr, F Reyes, SJ Bame,
1419 and HW Moos. Correlated variations of uv and radio emissions during an outstanding
1420 jovian auroral event. *Journal of Geophysical Research: Planets (1991–2012)*, 98(E10):
1421 18779–18791, 1993.
- 1422 Renée Prangé, Laurent Pallier, Kenneth C Hansen, Russ Howard, Angelos Vourlidas,
1423 Régis Courtin, and Chris Parkinson. An interplanetary shock traced by planetary
1424 auroral storms from the sun to saturn. *Nature*, 432(7013):78–81, 2004.
- 1425 P Prikryl, RA Greenwald, GJ Sofko, JP Villain, CWS Ziesolleck, and E Friis-Christensen.
1426 Solar-wind-driven pulsed magnetic reconnection at the dayside magnetopause, pc5 com-
1427 pressional oscillations, and field line resonances. *Journal of Geophysical Research: Space*
1428 *Physics (1978–2012)*, 103(A8):17307–17322, 1998.
- 1429 Wayne R Pryor, A Ian F Stewart, Larry W Esposito, William E McClintock, Joshua E
1430 Colwell, Alain J Jouchoux, Andrew J Steffl, Donald E Shemansky, Joseph M Ajello,
1431 Robert A West, et al. Cassini uvis observations of jupiter’s auroral variability. *Icarus*,
1432 178(2):312–326, 2005.
- 1433 E Robbrecht, D Berghmans, and RAM Van der Linden. Automated lasco cme catalog
1434 for solar cycle 23: are cmes scale invariant? *The Astrophysical Journal*, 691(2):1222,
1435 2009a.

- 1436 Eva Robbrecht, Spiros Patsourakos, and Angelos Vourlidas. No trace left behind: Stereo
1437 observation of a coronal mass ejection without low coronal signatures. *The Astrophysical*
1438 *Journal*, 701(1):283, 2009b.
- 1439 MGGT Taylor, H Hasegawa, B Lavraud, T Phan, CP Escoubet, MW Dunlop, YV Bog-
1440 danova, AL Borg, M Volwerk, J Berchem, et al. Spatial distribution of rolled up kelvin-
1441 helmholtz vortices at earth's dayside and flank magnetopause. In *Annales Geophysicae*,
1442 volume 30, pages 1025–1035, 2012.
- 1443 MF Thomsen, DB Reisenfeld, DM Delapp, RL Tokar, DT Young, FJ Crary, EC Sittler,
1444 MA McGraw, and JD Williams. Survey of ion plasma parameters in saturn's mag-
1445 netosphere. *Journal of Geophysical Research: Space Physics (1978–2012)*, 115(A10),
1446 2010.
- 1447 LM Trafton, V Dols, J-C Gérard, JH Waite Jr, GR Gladstone, and Guy Munhoven.
1448 Hst spectra of the jovian ultraviolet aurora: Search for heavy ion precipitation. *The*
1449 *Astrophysical Journal*, 507(2):955, 1998.
- 1450 Marissa F Vogt, Margaret G Kivelson, Krishan K Khurana, Raymond J Walker, Bertrand
1451 Bonfond, Denis Grodent, and Aikaterini Radioti. Improved mapping of jupiter's auroral
1452 features to magnetospheric sources. *Journal of Geophysical Research: Space Physics*
1453 *(1978–2012)*, 116(A3), 2011.
- 1454 Marissa F Vogt, Emma J Bunce, Margaret G Kivelson, Krishan K Khurana, Raymond J
1455 Walker, Aikaterini Radioti, Bertrand Bonfond, and Denis Grodent. Magnetosphere-
1456 ionosphere mapping at jupiter: Quantifying the effects of using different internal field
1457 models. *Journal of Geophysical Research: Space Physics*, 2015.

- 1458 JH Waite, F Bagenal, F Seward, C Na, GR Gladstone, TE Cravens, KC Hurley, JT Clarke,
1459 R Elsner, and SA Stern. Rosat observations of the jupiter aurora. *Journal of Geophysical*
1460 *Research: Space Physics (1978–2012)*, 99(A8):14799–14809, 1994.
- 1461 JH Waite, GR Gladstone, WS Lewis, R Goldstein, DJ McComas, P Riley, RJ Walker,
1462 P Robertson, S Desai, JT Clarke, et al. An auroral flare at jupiter. *Nature*, 410(6830):
1463 787–789, 2001.
- 1464 R. J. Wilson, P. A. Delamere, F. Bagenal, and A. Masters. Kelvin-helmholtz instability
1465 at saturn’s magnetopause: Cassini ion data analysis. *Journal of Geophysical Research:*
1466 *Space Physics*, 117(A3):n/a–n/a, 2012. ISSN 2156-2202. doi: 10.1029/2011JA016723.
1467 URL <http://dx.doi.org/10.1029/2011JA016723>. A03212.
- 1468 RJ Wilson and MK Dougherty. Evidence provided by galileo of ultra low frequency waves
1469 within jupiter’s middle magnetosphere. *Geophysical research letters*, 27(6):835–838,
1470 2000.
- 1471 Philippe Zarka. Auroral radio emissions at the outer planets: Observations and theories.
1472 *Journal of Geophysical Research: Planets (1991–2012)*, 103(E9):20159–20194, 1998.
- 1473 Bertalan Zieger and Kenneth C Hansen. Statistical validation of a solar wind propagation
1474 model from 1 to 10 au. *Journal of Geophysical Research: Space Physics (1978–2012)*,
1475 113(A8), 2008.

Figure 1. mSWiM propagation model [Zieger and Hansen, 2008] at Jupiter on a given Day of Year in 2011. From top to bottom: solar wind density, velocity and the B_T magnetic field component. Start/end times of Chandra X-ray observations are shown by dashed lines for the first (red) and second (blue) observation (see text for details). The 10-15 hour uncertainty in the model is indicated by the black bar towards the top of each parameter plot.

Figure 2. STEREO A (upper) and B (lower) Power Spectral Density plot of the radio emission, shifted for Jupiter-Earth light travel-time (UT-34 minutes). ‘Non-Io’ indicates bursts of non-Io decametric radio emission that suggest the arrival of a forward shock at Jupiter [Hess et al., 2012, 2014]. ‘Io’ indicates Io decametric radio emission associated with activity from Io. The black horizontal arrows indicate the timings of the Chandra X-ray observations. The first non-Io decametric burst occurs 0.1 DoY before the end of the first Chandra observation, suggesting a forward shock arrived at Jupiter during the first X-ray observation.

Figure 3. System III (S3) coordinate projections onto Jupiter’s geographic North Pole (plot centre) for the first observation(left), during which the ICME arrived at Jupiter and the second observation (right), 1.2 days later. Lines of constant Jovian S3 longitude radiate outwards from the pole, increasing clockwise in increments of 30° from 0° at the bottom of the projection. Concentric dotted circles outwards from the pole represent lines of 80° , 70° , 60° and 30° latitude. The alternate green and black contours, indicate VIP4 model magnetic field strength in Gauss. The outer red oval is the Grodent et al. [2008] contour of Io’s footprint ($5.8R_J$). The inner red contour is the footprint for the $30 R_J$ field line from Vogt et al. [2011] mapping using the Grodent et al. [2008] anomaly model. The thick orange contour is the average location of the UV main oval from two HST observation campaigns in 2007 [Nichols et al., 2009]. The projections show more X-ray events in the hot spot (160° - 180° S3 longitude, 60° - 70° latitude) during the first observation than the second. The events appear to spread from the hot spot into the region from 150° - 160° . More clearly identifiable is the bright change in emission in the auroral enhancement quadrant (180° - 270° S3 longitude, 55° - 90° latitude). The distribution of this emission is not only enhanced in the main oval, but also poleward of this and at lower latitudes near Io’s magnetic footprint.

Figure 4. Number of events in 5° latitude bins during the first (blue) and second (red) observations. Upper plot: Hot Spot Quadrant with S3 longitudes $90^\circ - 180^\circ$. Lower plot: Auroral Enhancement Quadrant with longitudes $180^\circ - 270^\circ$. For the Auroral Enhancement Quadrant, emission above 60° latitude is up to 5 times brighter in the first observation than the second. Error bars are calculated from Poisson statistics. At the time of maximum visibility, each quadrant above 60° latitude had a projected area of $\sim 3\%$ of the total observable Jovian disk.

Figure 5. X-ray aurora lightcurves for the first (top) and second (bottom) observation. Blue line: X-rays in the Hot Spot Quadrant (S3 longitude: $90-180^\circ$). Red line: X-rays in the Auroral Enhancement Quadrant (S3 longitude: $180-270^\circ$). The light curves were generated by placing events above 60° latitude in S3 coordinates into 1 minute bins. These were then shifted to account for Jupiter-Earth light travel-time of 34 minutes (UT - 34 minutes). The sub-solar longitude at the time of the observations is indicated along the top of each plot. The green vertical dashed line indicates the onset of the brightest burst of non-*Io* decametric emission in the STEREO A data. The projected area of each quadrant (as a percentage of the total area of Jupiter) is indicated by the blue (HSQ) and red (AEQ) dashed lines. At the point of maximum visibility each quadrant above 60° latitude takes up a projected area that is $\sim 3\%$ of the total observable Jovian disk.

Figure 6. The Northern Auroral Zone spectra for the first (upper) and second observation (lower). The Hot Spot Quadrant spectra are on the left (a,b), while the Auroral Enhancement Quadrant are on the right (c,d). The data have been fitted with a combination of lines with half widths fixed at 20 eV.

Figure 7. Comparisons of North Pole S3 projections for discrete energy ranges for the first (left) and second (right) observations. From top to bottom the energy ranges are: a) 200-500eV (carbon/sulfur ion lines), b) 500-800eV (oxygen ion lines), c) 800-1500eV (Dominated by fluoresced and scattered solar photons), d) 1500-5000eV (Hard X-ray bremsstrahlung radiation from electrons). For further plot details see figure 3.

Figure 8. Latitude-counts plots for 5° latitude bins. Comparisons of the 200-500eV carbon/sulfur emission (upper 2 plots) or 500-800eV oxygen emission (lower 2 plots) between the first observation (blue line) and second observation (red line). The Hot Spot Quadrant (left) and Auroral Enhancement Quadrant (right) are treated separately. At the time of maximum visibility, each quadrant had a projected area of $\sim 3\%$ of the total observable Jovian disk.

Figure 9. S3 Polar Projections showing X-ray emission coinciding with specific sub-solar longitudes (SSL). Each plot shows emission that occurred at times when the SSL was $\pm 15^\circ$ from the SSL stated (120° in this case). The Sun's direction (noon) lies along the red arrow, with dawn 90° clockwise from this and dusk 90° anti-clockwise. A Vogt et al. [2011] mapping using a Grodent Anomaly Model [Grodent et al., 2008], assuming an expanded magnetosphere, is plotted onto this polar projection. The plot shows closed field lines increasing in increments of $5R_J$ from the $15 R_J$ contour (red), through 50 - $80 R_J$ contours (yellow), to the last closed contour at the nose of an expanded magnetosphere $90 R_J$ (inner green contour). Green contours map to $95 - 150 R_J$. The thick purple contour indicates the predicted open-closed field line boundary. Regions poleward of this and absent of contours indicate regions mapping to open field lines. Events occurring close to the noon position have uncertainties in their spatial position of $\sim 5^\circ$ latitude-longitude, while those occurring closer to dawn or dusk originate on the limb and have uncertainties of $\sim 10^\circ$ - 20° latitude-longitude. Emission is colour coded: carbon/sulfur photons (red), oxygen photons (blue), solar X-rays photons (grey), Hard X-rays from electrons (green). carbon/sulfur emission can be found mostly on contours mapping to 50 - $90 R_J$ and also clustered in the open field line region. Oxygen emission is mostly on contours of 70 - $120 R_J$ and in open field line regions. The Hard X-rays from electrons can be found clustered on the dawn edge of the projection.

Figure 10. S3 Polar Projections of the first observation, binned based on sub-solar longitude (SSL). Vogt et al. [2011] expanded magnetosphere models are plotted onto the polar projections. Throughout the observation, emission appears to exhibit a local time dependence and may follow the open-closed field line boundary. The time-bins at 270° and 300° SSL show the auroral enhancement event. Each dot is an X-ray photon. For further plot details see figure 9.

Figure 11. S3 Polar Projections of the second observation, binned based on sub-solar longitude (SSL), with Vogt et al. [2011] expanded magnetosphere models. Each dot is an X-ray photon. For further plot details see figure 9.

Figure 12. Sub-solar Longitude (SSL) binned polar projections comparing compressed (left) and expanded (right) magnetosphere models for the hot spot during the first observation. Projections for SSL of 120° (upper), 150° (middle) and 210° (lower) are shown. The models use Joy et al. [2002] measurements of the magnetopause distance. The compressed model uses a noon magnetopause at $63R_J$, while the expanded model, assumes a noon magnetopause at $92R_J$. The field lines increase in increments of $5R_J$ from the outer contour of $15R_J$ (red), to the final closed inner contour of 65 (yellow - left plots) or 95 (green- right plots). For colour coding and plot details see figure 9.

Figure 13. Sub-solar Longitude (SSL) binned polar projections for the hot spot for the first (left) and second (right) observation, using an expanded magnetosphere model for both. For colour coding and details see figure 9.

Figure 14. Sub-solar Longitude (SSL) binned polar projections for the auroral enhancement for the first (left) and second (right) observations, using the expanded magnetosphere model for both. The Auroral Enhancement occurs in the 270° SSL plot. For colour coding and plot details see figure 9.

Author Manuscript

Figure 15. Power spectral density (PSD) plots showing periodicity in the hot spot: a) Observation 1 (ICME Arrival), b) Observation 2 (ICME Recovery), c) Observation 1 sulfur/carbon (200-500 eV) photons, d) Observation 1 oxygen (500-800 eV) photons. During the first observation two periods were detected at 12 and 26 minutes. The 26 minute peak was more significant than the 45minute period reported by Gladstone et al. [2002]. The second observation contains a less distinctive periodicity, with the most prominent period at 42 minutes. The hot spot region was found to be much broader during the first observation, so a different region was used for each PSD to maximise the significance of the periods and to utilise as much emission from the expanded hot spot as possible (see text for details). Carbon/Sulfur emissions are dominated by the 26 minute period and also feature a less significant 12 minute period. The oxygen emissions feature no 26 minute, but do feature the less significant 12 minute period. When the two populations are combined the 12 minute period becomes much more significant. The dotted horizontal lines show single-frequency probabilities of chance occurrence (PCO) for the detected periods [Leahy et al. 1983]. The lowest statistical significance and therefore highest PCO of 10^{-1} is at the bottom of the plot and the highest statistical significance and therefore lowest PCO of 10^{-6} is towards the top of the plot.

Figure 16. Summary of X-ray source mapping (not to scale) accounting for uncertainties in photon spatial mapping. The x-axis indicates the equatorial radial distance from Jupiter that the source regions map to. The different X-ray regions are indicated by the striped blocks: the Hard X-ray region (green), the region dominated by high charge state sulfur region (red) and the mixed high charge state carbon/sulfur and oxygen region (red and blue).

Author Manuscript

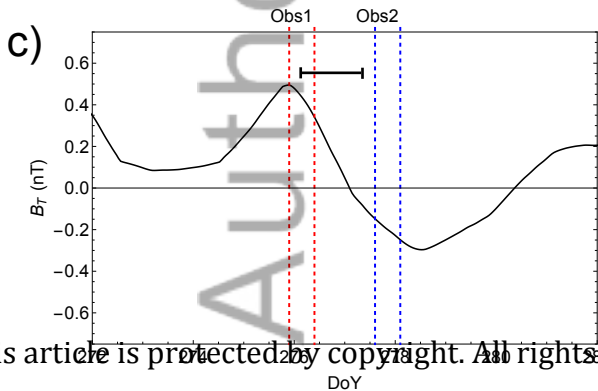
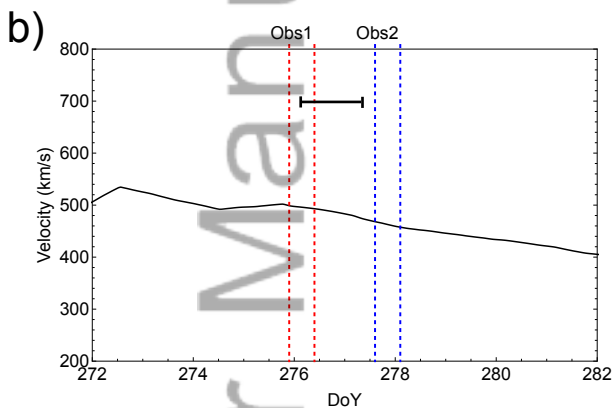
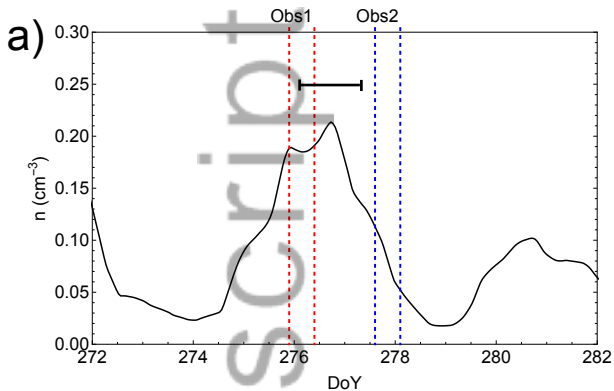
1st Observation Hot Spot Quadrant – Reduced $\chi^2 \sim 0.45$ (105 Degrees of Freedom)		
Best Fit Line, eV	Flux, Photons/cm ² /s	Known Ion Rest Frame Energies
310±10	$5 \pm 1 \times 10^{-4}$	S VI-X (260-291;314;316 eV) or C V (299;304-308 eV)
595±20	$1.5 \pm 0.5 \times 10^{-5}$	O VII (561;568;574 eV)
730±35	$6.5 \pm 3 \times 10^{-6}$	O VII (698-713 eV) or O VIII (774 eV)
860±30	$4.5 \pm 1.5 \times 10^{-6}$	O VIII (836 eV) or Solar Fe XVII (812;826 eV)
990±60	$1.5 \pm 1 \times 10^{-6}$	Solar Ne X + Fe XXI (~ 1000 eV)
1140±85	$9 \pm 6 \times 10^{-7}$	Solar Ne X + Fe XXI (~ 1000 eV)
1375±60	$1 \pm 0.5 \times 10^{-7}$	Solar Mg XI (1350 eV)

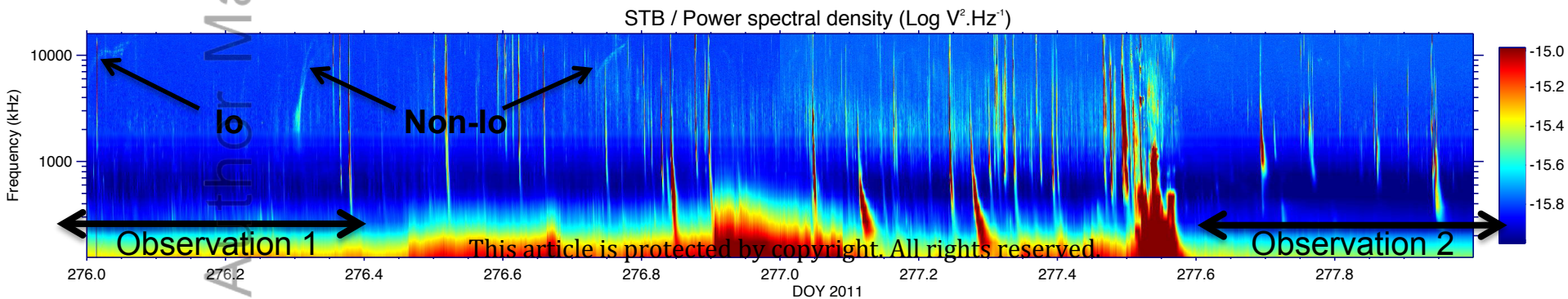
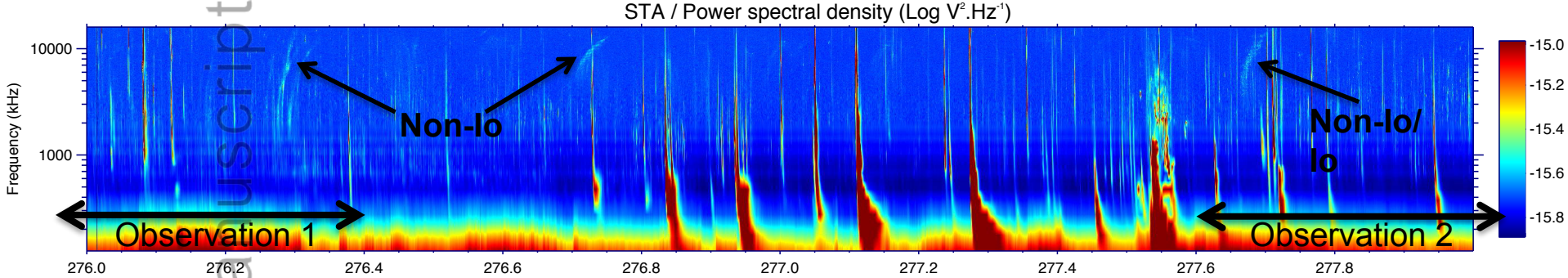
2nd Observation Hot Spot Quadrant – Reduced $\chi^2 \sim 0.4$ (111 Degrees of Freedom)		
Best Fit Line, eV	Flux, Photons/cm ² /s	Known Ion Rest Frame Energies
310±10	$4.5 \pm 1 \times 10^{-4}$	S VI-X (260-291 eV) or C V (299;304-308 eV)
610±50	$9 \pm 5 \times 10^{-6}$	O VII (561;568;574 eV) or O VIII (654 eV)
700±35	$8.5 \pm 5.5 \times 10^{-6}$	O VII (698-713 eV)
925±25	$4 \pm 1 \times 10^{-6}$	Solar Ne X + Fe XXI (~ 1000 eV)

1st Observation Aurora Enhancement Quadrant – Reduced $\chi^2 \sim 0.6$ (109 Degrees of Freedom)		
Best Fit Line, eV	Flux, Photons/cm ² /s	Known Ion Rest Frame Energies
305^{+10}_{-100}	$3 \pm 2 \times 10^{-4}$	S VI-X (260-291 eV) or C V (299;304-308 eV)
390±60	$4.5 \pm 3 \times 10^{-5}$	S IX- S XIV (336-348;380 eV) or C V-VI (354-378)
590±15	$1.5 \pm 0.5 \times 10^{-5}$	O VII (561;568;574 eV)
775±20	$7 \pm 2 \times 10^{-6}$	O VIII (774 eV)
915±65	$1.5 \pm 2 \times 10^{-6}$	Solar Ne X + Fe XXI (~ 1000 eV)

2nd Observation Aurora Enhancement Quadrant – Reduced $\chi^2 \sim 0.55$ (111 Degrees of Freedom)		
Best Fit Line, eV	Flux, Photons/cm ² /s	Known Ion Rest Frame Energies
310±10	$2 \pm 1 \times 10^{-4}$	S VI-X (260-291 eV) or C V (299;304-308 eV)
645±40	$7 \pm 2.5 \times 10^{-6}$	O VII (665 eV) or O VIII (654 eV;698-713 eV)
875±60	$2 \pm 1 \times 10^{-6}$	O VIII (836 eV) or Fe XXI + Ne X (~ 1000 eV)
1095±65	$1 \pm 0.5 \times 10^{-6}$	Solar Ne X + Fe XXI (~ 1000 eV)

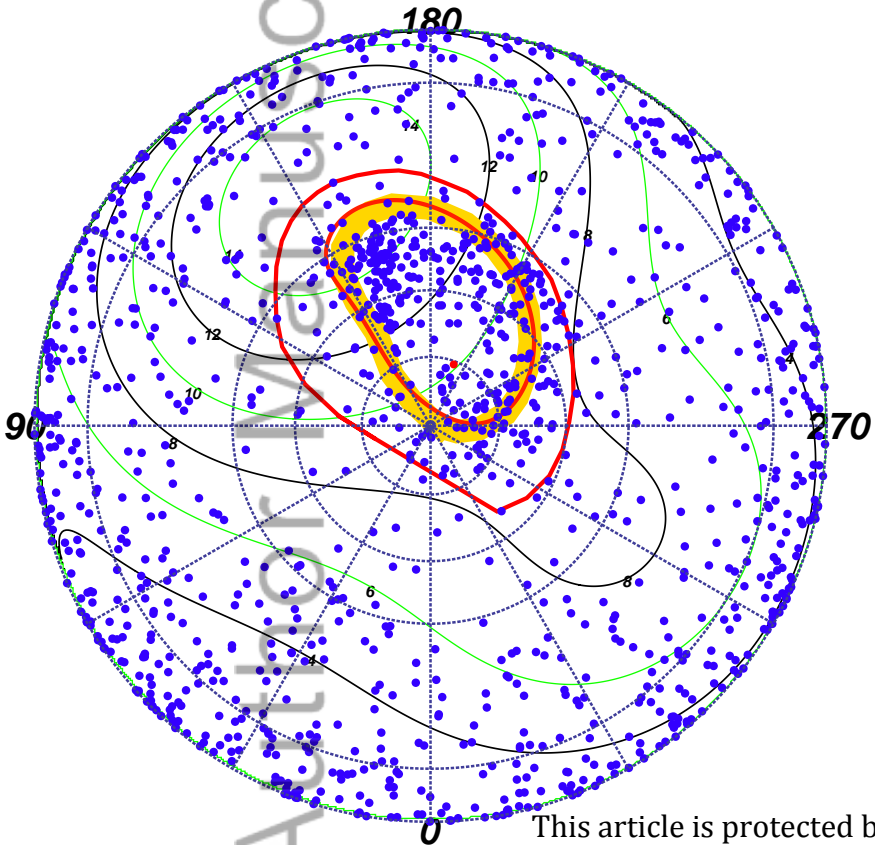
Table 1. Best fit parameters for the 0.24–2 keV spectra and closest known ion rest frame lines [Elsner et al., 2005; Kharchenko et al., 2008; Branduardi-Raymont et al., 2007b] Line half widths were held constant at 20 eV.



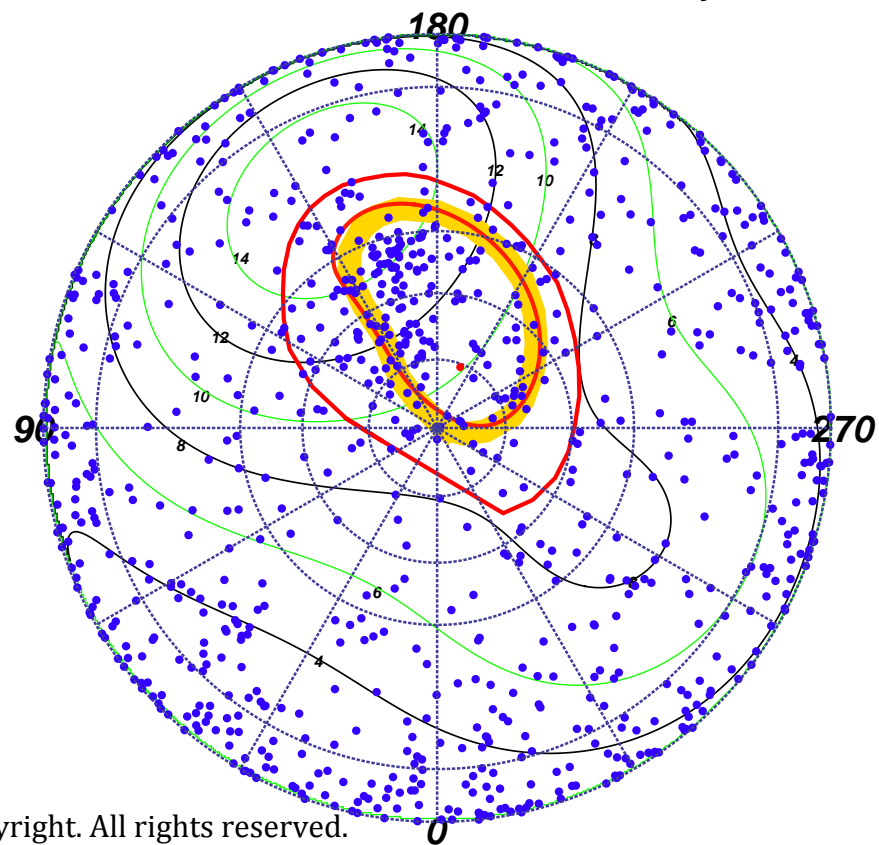


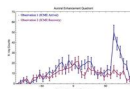
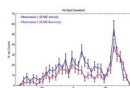
North Pole X-ray Projections

Observation 1 (ICME Arrival)



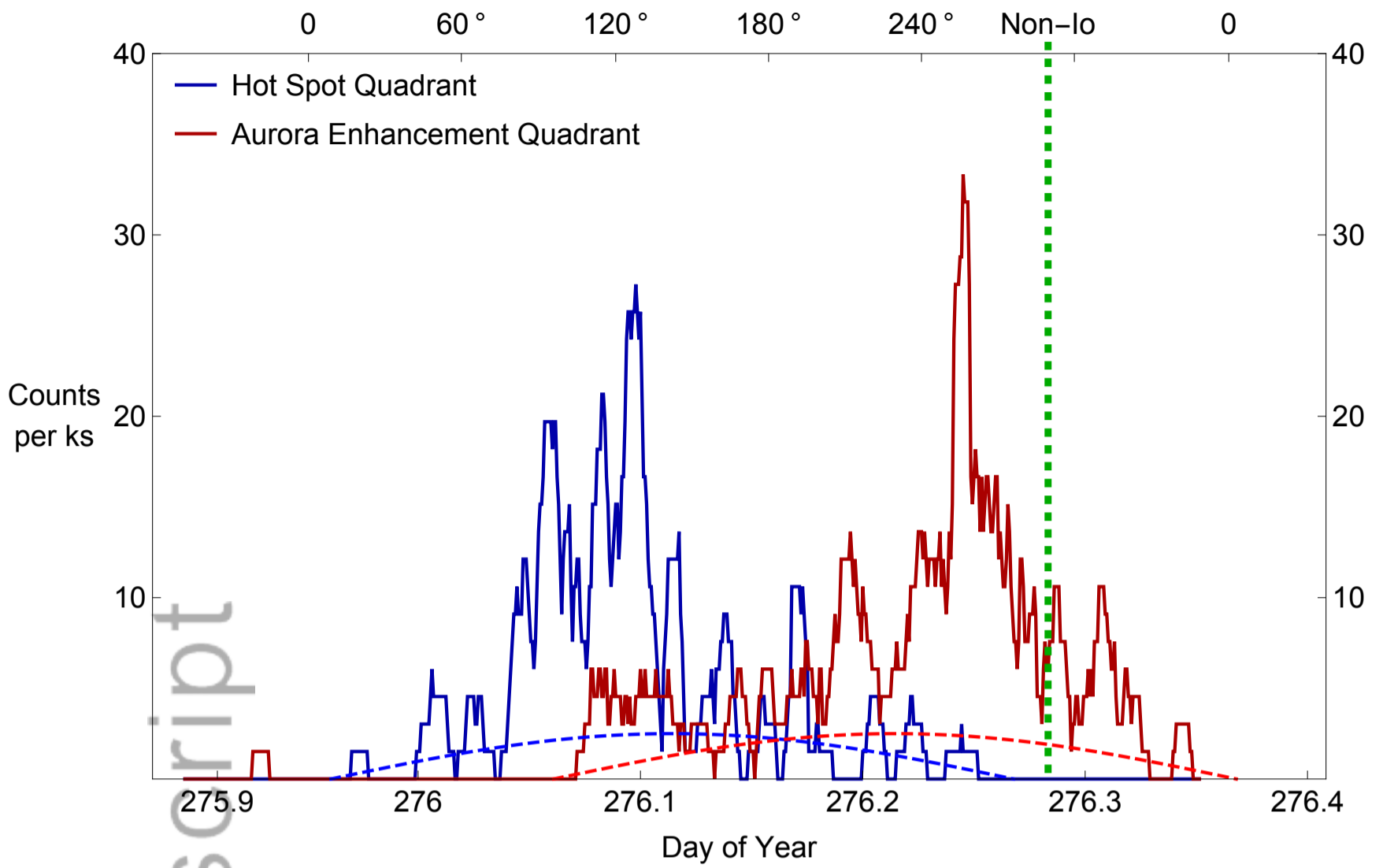
Observation 2 (ICME Recovery)



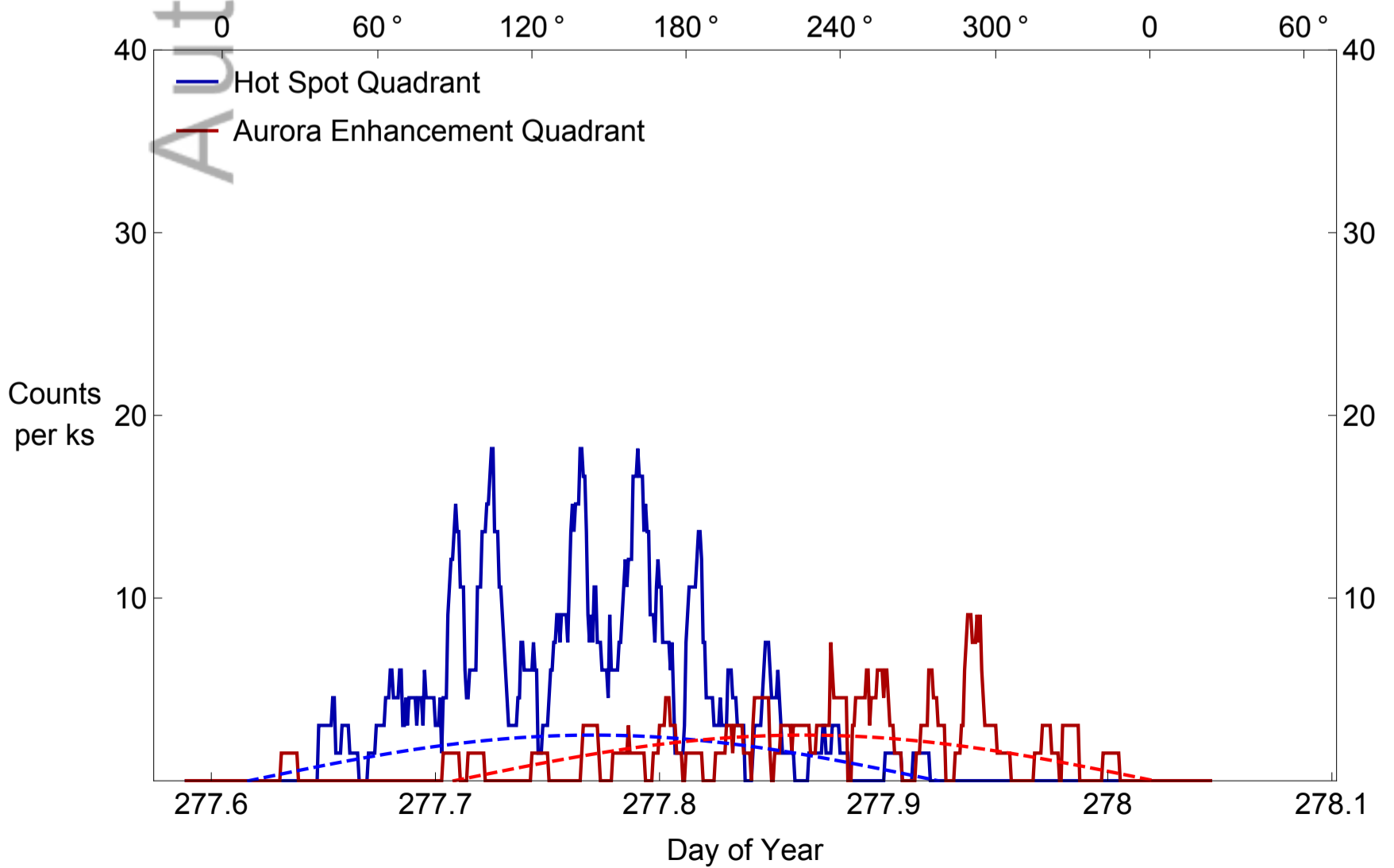


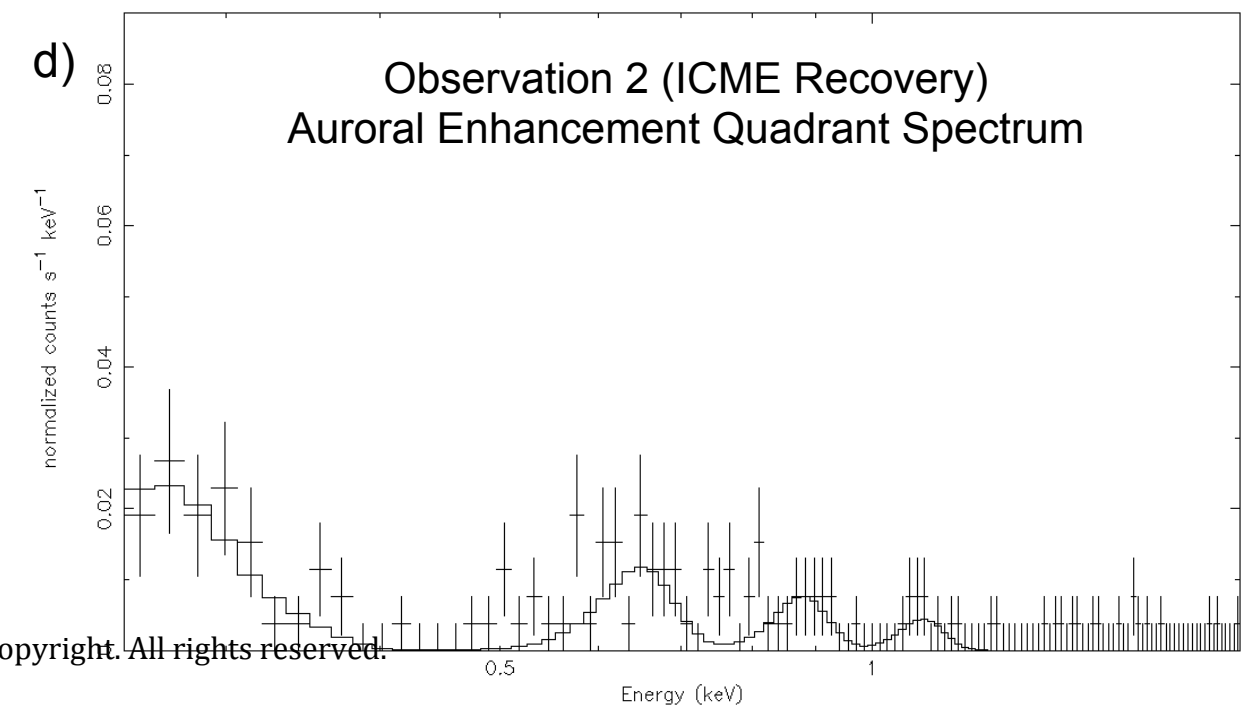
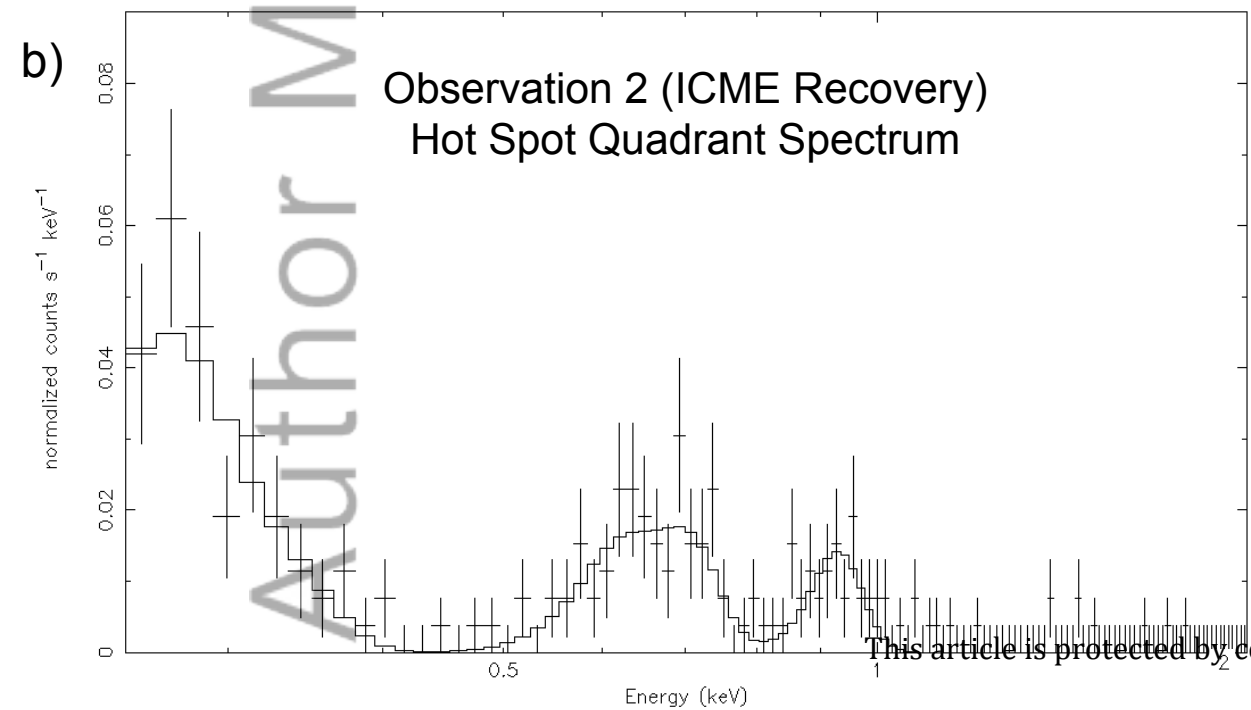
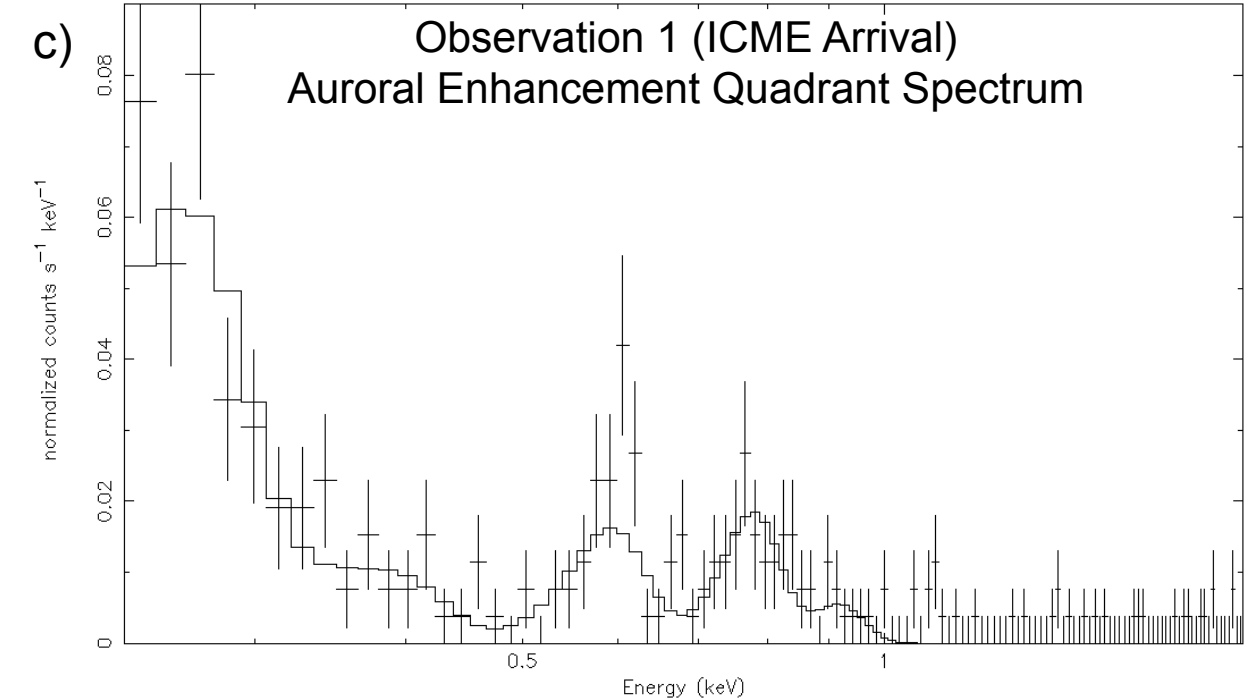
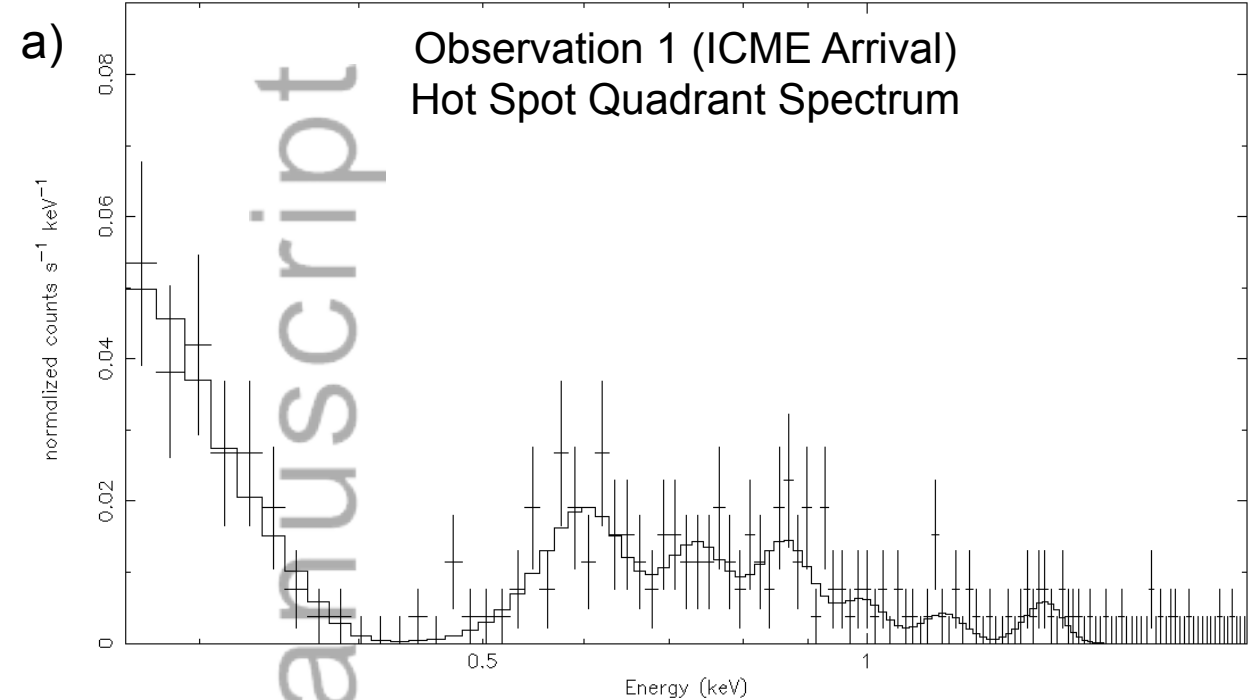
2015JA021888-f03-z-.jpg

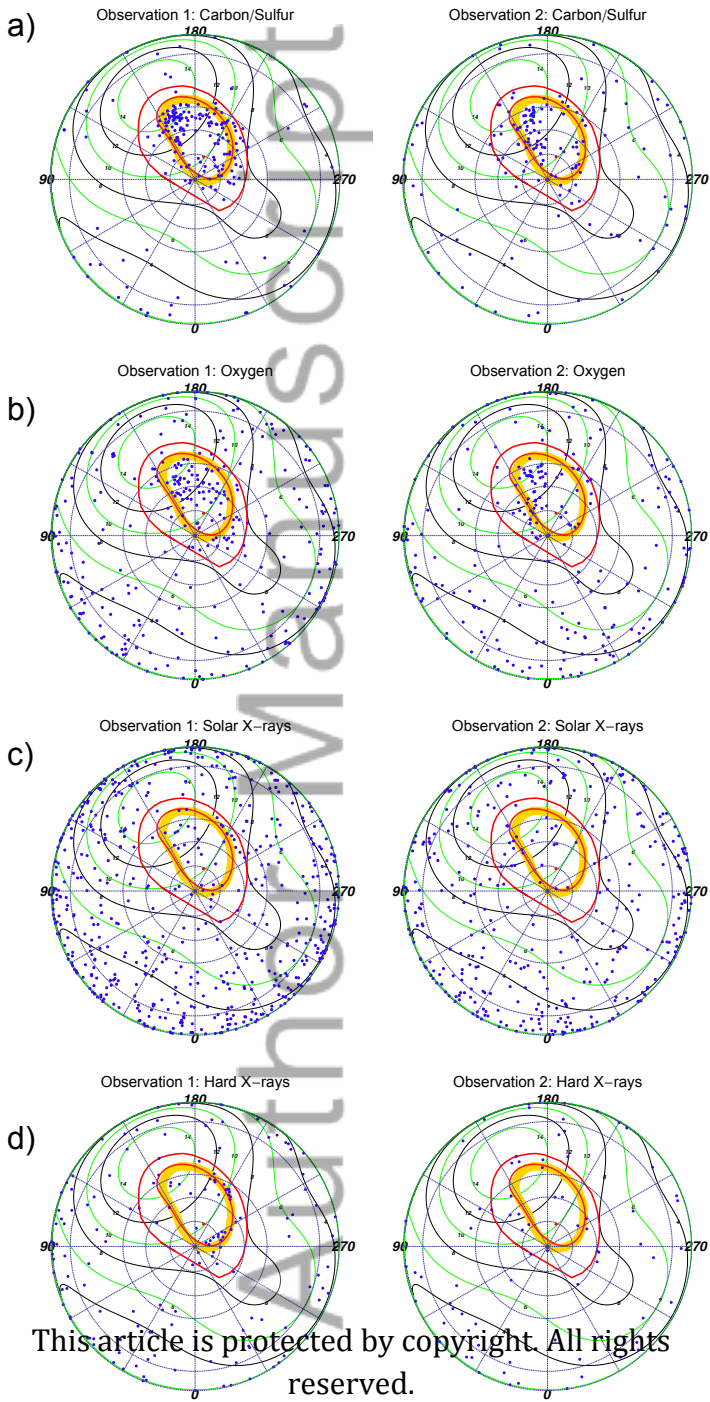
First Observation (ICME Arrival): HSQ and AEQ Lightcurves

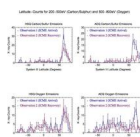


Second Observation (ICME Recovery): HSQ and AEQ Lightcurves

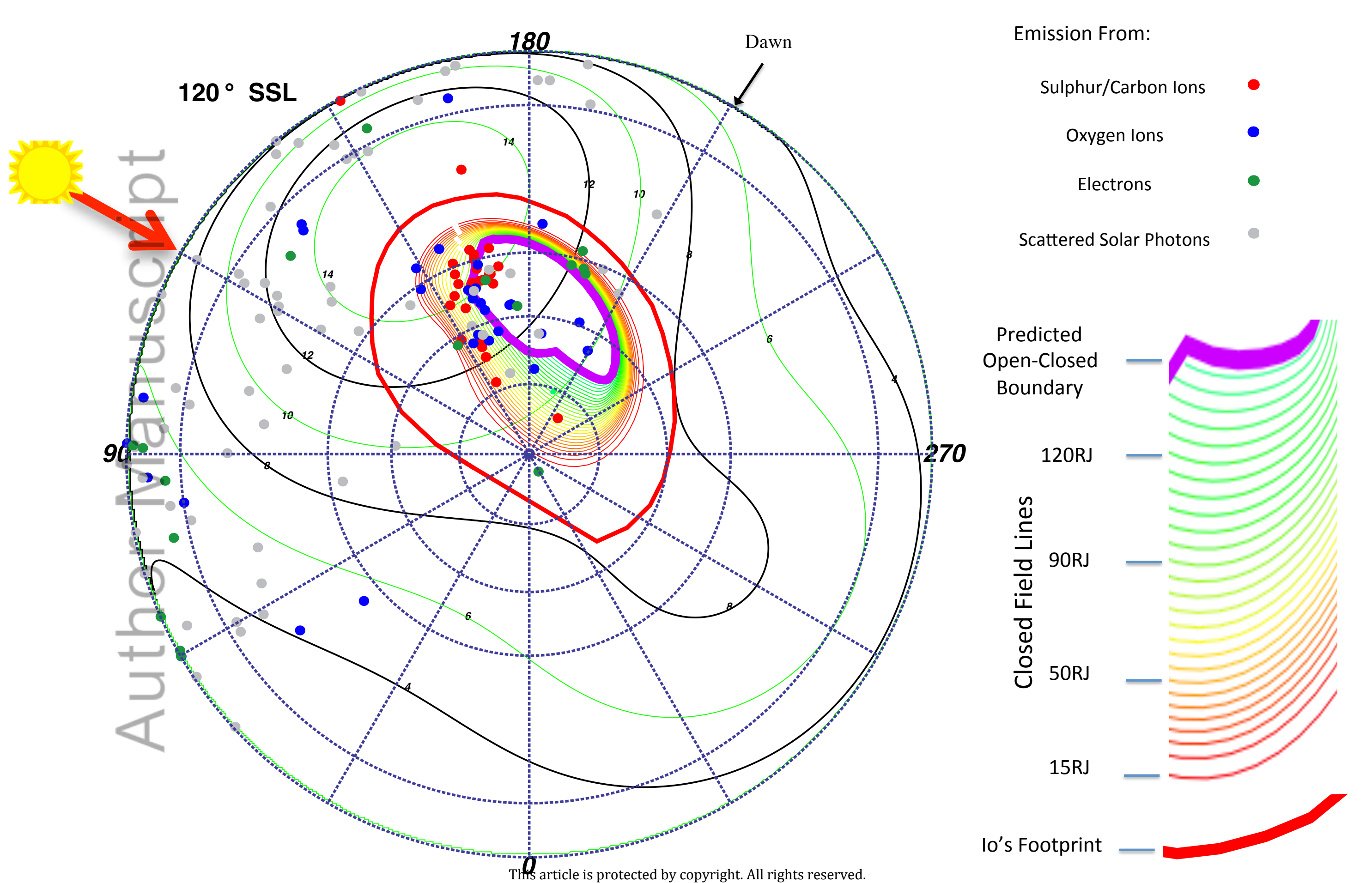




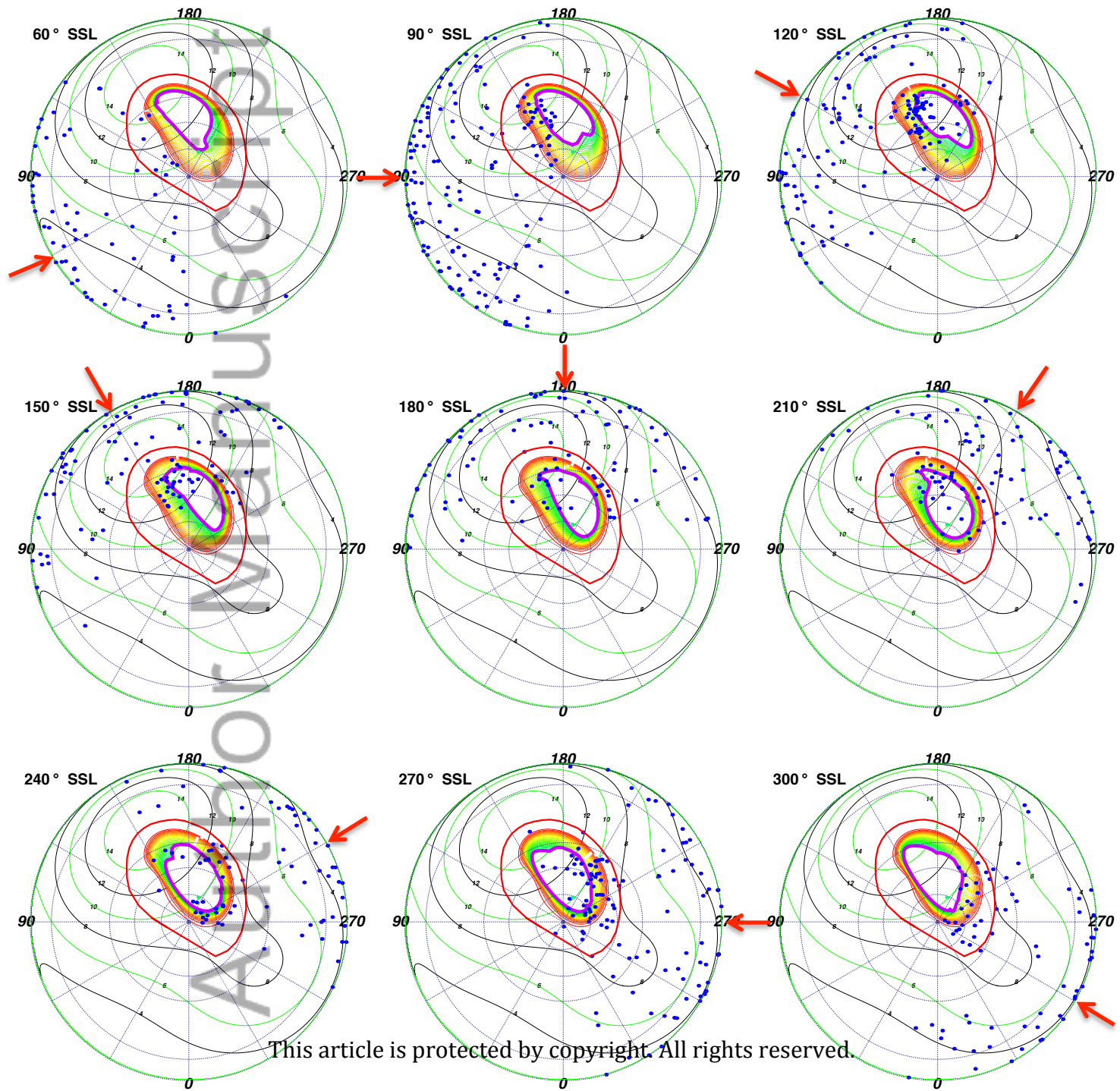




2015JA021888-f07-z-.jpg

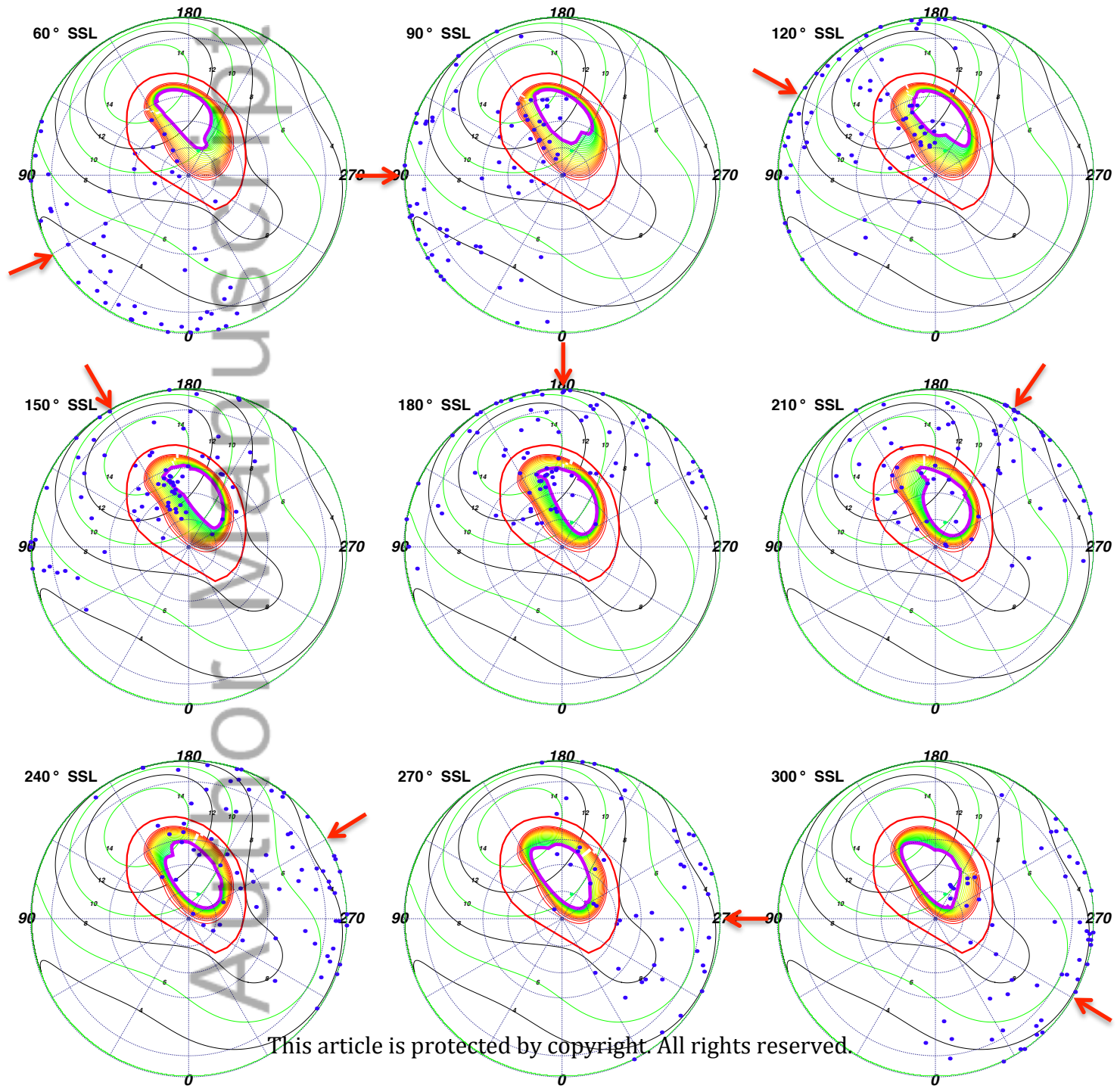


Observation 1 (ICME Arrival)



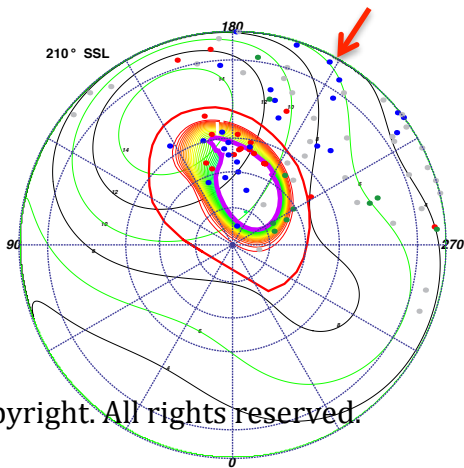
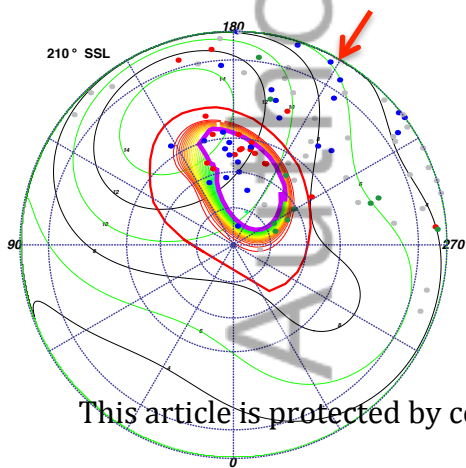
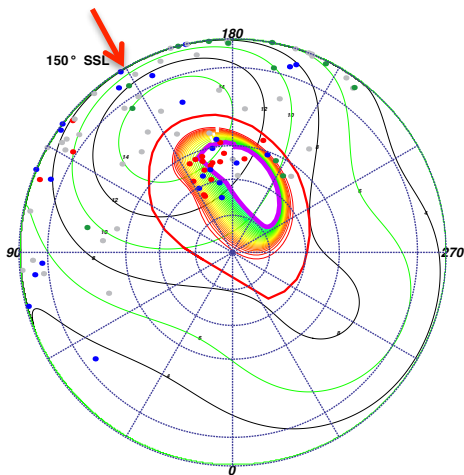
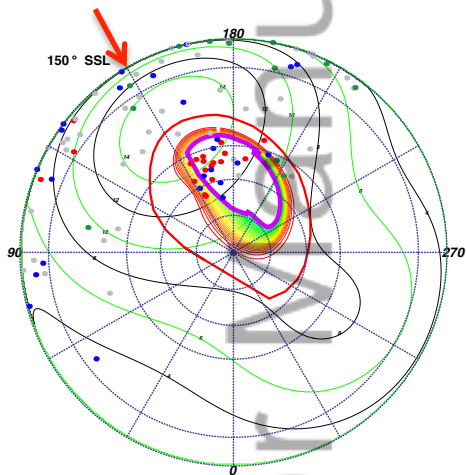
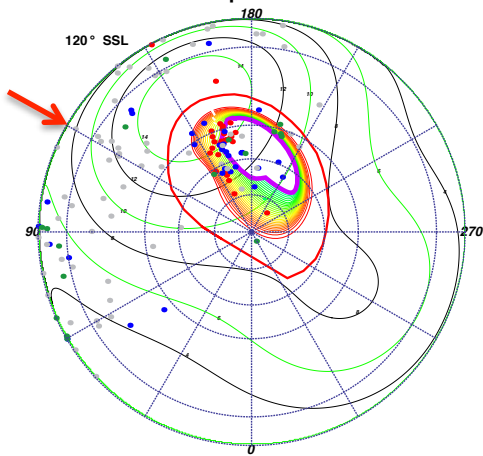
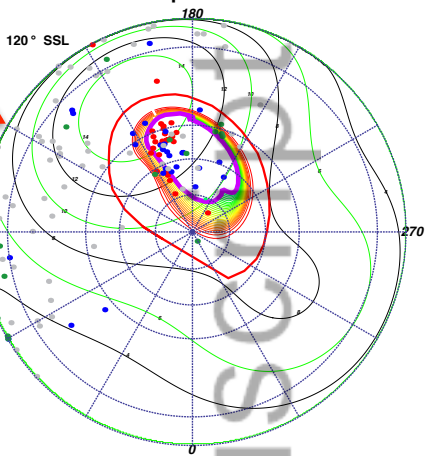
This article is protected by copyright. All rights reserved.

Observation 2 (ICME Recovery)



Compressed

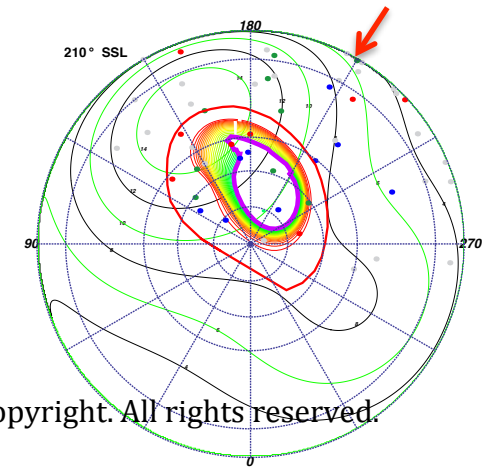
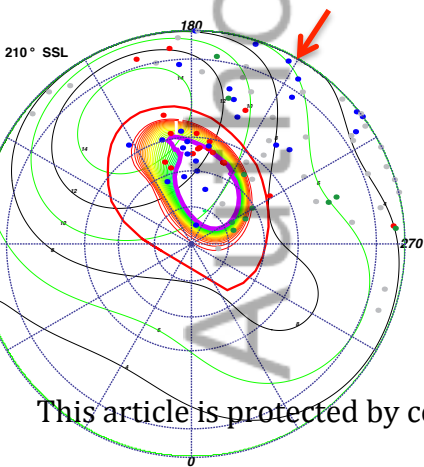
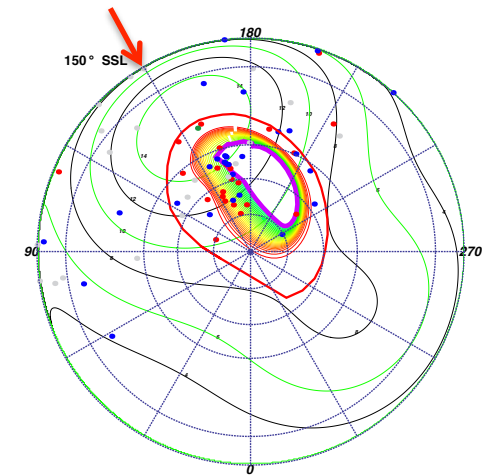
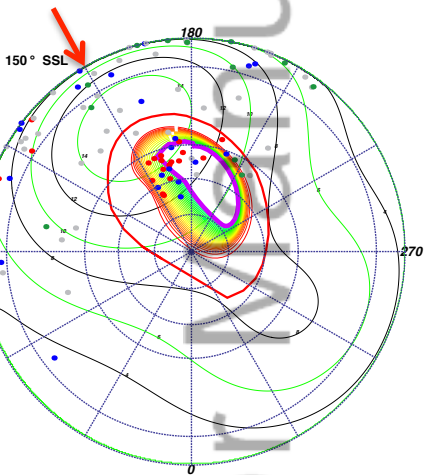
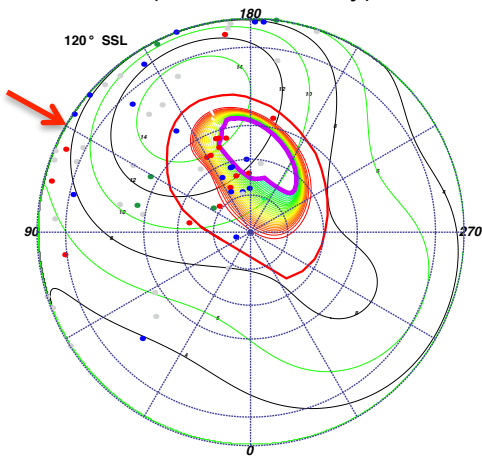
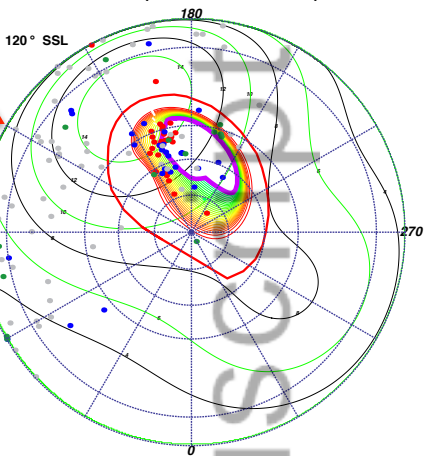
Expanded



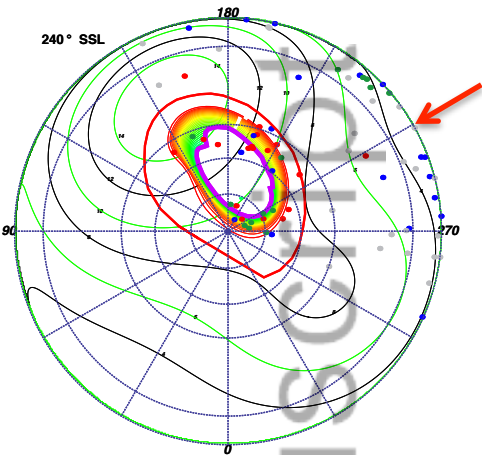
This article is protected by copyright. All rights reserved.

Obs 1 (ICME Arrival)

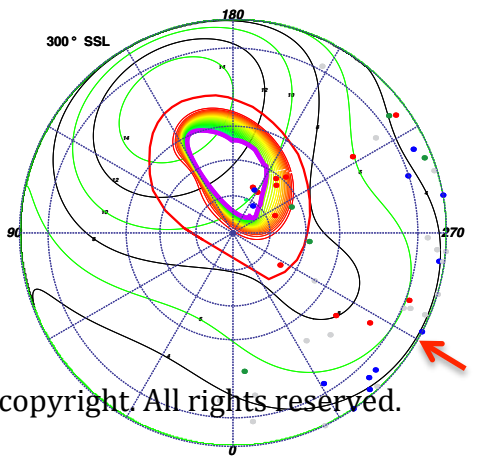
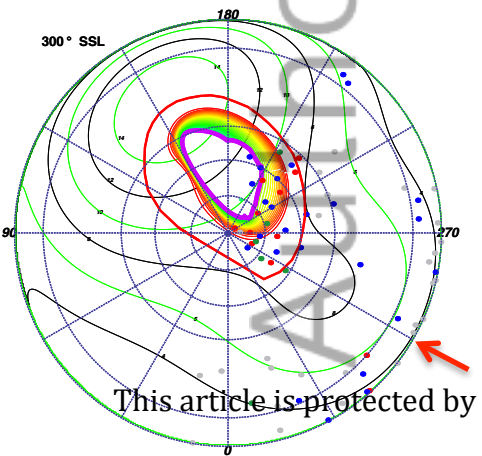
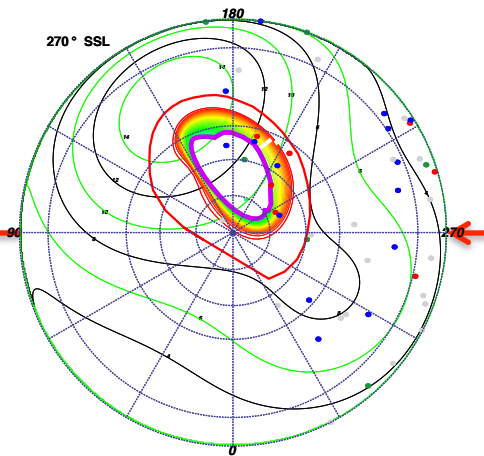
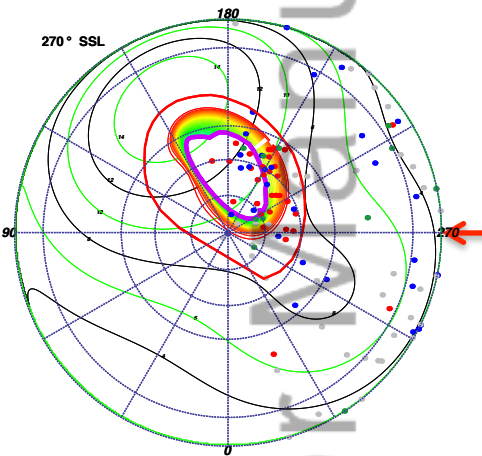
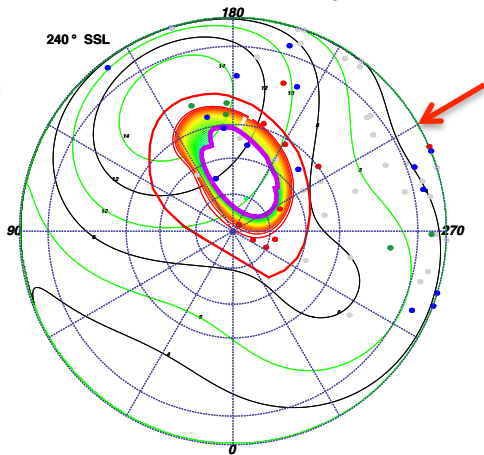
Obs 2 (ICME Recovery)



Obs 1 (ICME Arrival)

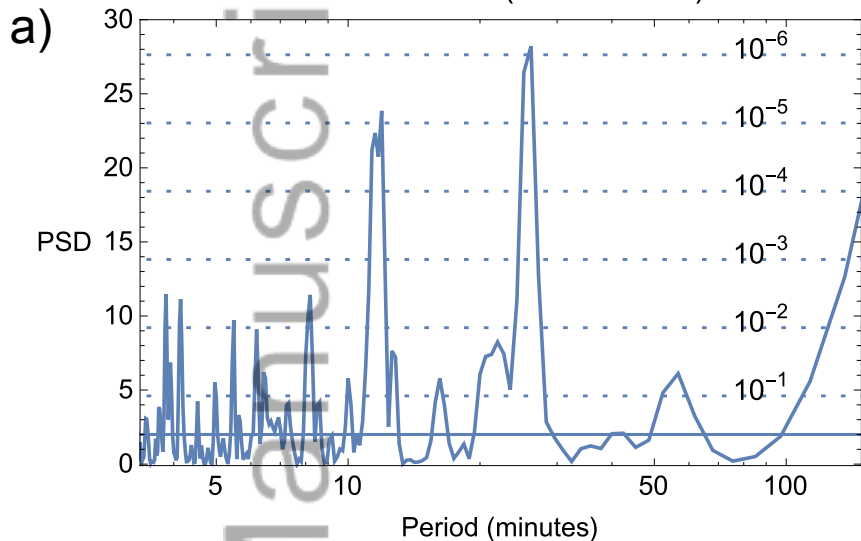


Obs 2 (ICME Recovery)

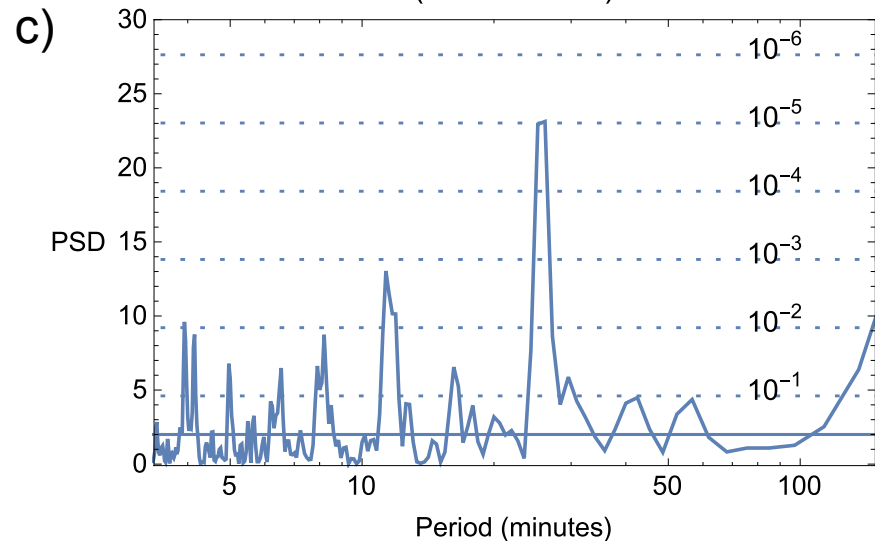


Hot Spot Periodicity

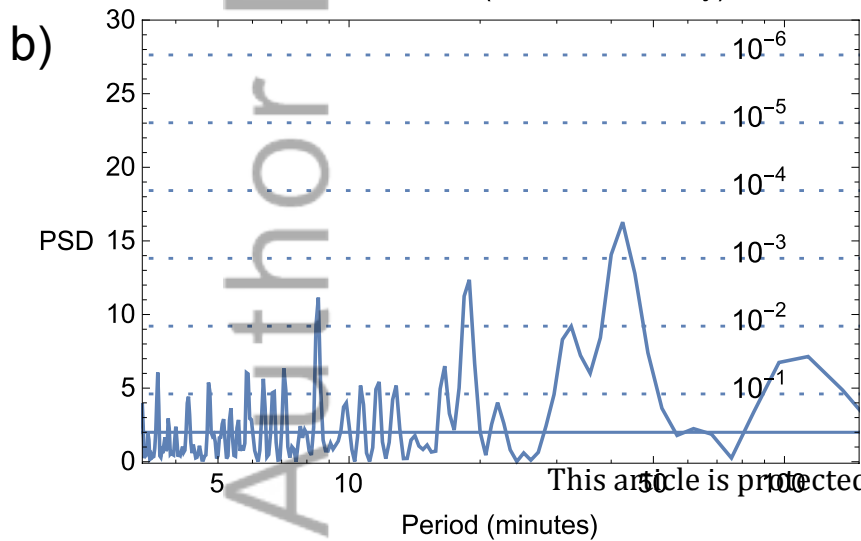
Observation 1 (ICME Arrival)



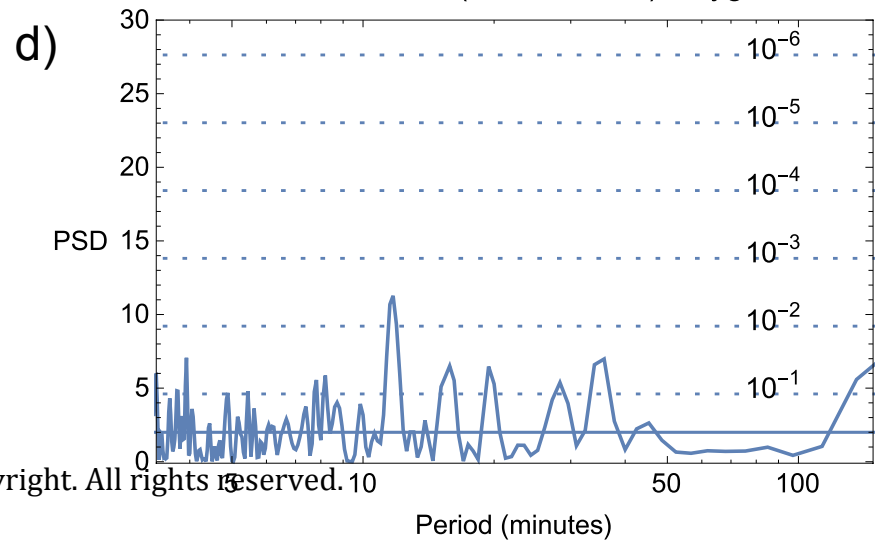
Observation 1 (ICME Arrival) Carbon/Sulfur



Observation 2 (ICME Recovery)



Observation 1 (ICME Arrival) Oxygen



Manuscript
Author

Jupiter Radial Equatorial Mapping of X-ray Features

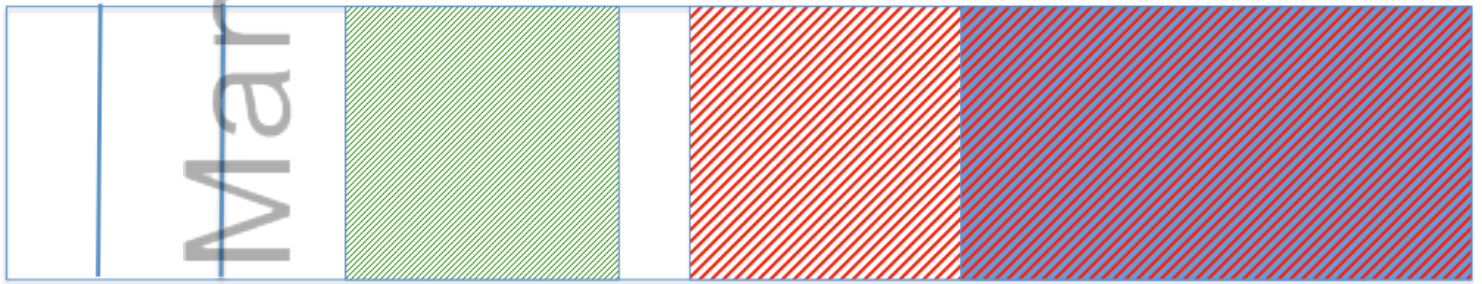
Auroral Emission:

Diffuse/Disk X-rays

Hard X-ray Region

Sulfur Dominated X-ray Region

Oxygen and Carbon/Sulfur X-ray Region



Increasing Radial Distance

Nose Magnetopause Location

2015JA021888-f15-z-.png